CONSTITUTIVE MODELING OF THE MALE PELVIC SYSTEM TO IMPROVE THE ACCURACY OF THE LOCATION OF NEOPLASMS IN MRI-TRUS FUSION PROSTATE BIOPSY

Muhammad Qasim

ADVERTIMENT. L'accés als continguts d'aquesta tesi doctoral i la seva utilització ha de respectar els drets de la persona autora. Pot ser utilitzada per a consulta o estudi personal, així com en activitats o materials d'investigació i docència en els termes establerts a l'art. 32 del Text Refós de la Llei de Propietat Intel·lectual (RDL 1/1996). Per altres utilitzacions es requereix l'autorització prèvia i expressa de la persona autora. En qualsevol cas, en la utilització dels seus continguts caldrà indicar de forma clara el nom i cognoms de la persona autora i el títol de la tesi doctoral. No s'autoritza la seva reproducció o altres formes d'explotació efectuades amb finalitats de lucre ni la seva comunicació pública des d'un lloc aliè al servei TDX. Tampoc s'autoritza la presentació del seu contingut en una finestra o marc aliè a TDX (framing). Aquesta reserva de drets afecta tant als continguts de la tesi com als seus resums i índexs.

ADVERTENCIA. El acceso a los contenidos de esta tesis doctoral y su utilización debe respetar los derechos de la persona autora. Puede ser utilizada para consulta o estudio personal, así como en actividades o materiales de investigación y docencia en los términos establecidos en el art. 32 del Texto Refundido de la Ley de Propiedad Intelectual (RDL 1/1996). Para otros usos se requiere la autorización previa y expresa de la persona autora. En cualquier caso, en la utilización de sus contenidos se deberá indicar de forma clara el nombre y apellidos de la persona autora y el título de la tesis doctoral. No se autoriza su reproducción u otras formas de explotación efectuadas con fines lucrativos ni su comunicación pública desde un sitio ajeno al servicio TDR. Tampoco se autoriza la presentación de su contenido en una ventana o marco ajeno a TDR (framing). Esta reserva de derechos afecta tanto al contenido de la tesis como a sus resúmenes e índices.

WARNING. Access to the contents of this doctoral thesis and its use must respect the rights of the author. It can be used for reference or private study, as well as research and learning activities or materials in the terms established by the 32nd article of the Spanish Consolidated Copyright Act (RDL 1/1996). Express and previous authorization of the author is required for any other uses. In any case, when using its content, full name of the author and title of the thesis must be clearly indicated. Reproduction or other forms of for profit use or public communication from outside TDX service is not allowed. Presentation of its content in a window or frame external to TDX (framing) is not authorized either. These rights affect both the content of the thesis and its abstracts and indexes.

UNIVERSITAT
ROVIRA i VIRGILI

Constitutive modeling of the male pelvic system to improve the accuracy of the location of neoplasms in MRI-TRUS fusion prostate biopsy

---

Muhammad Qasim

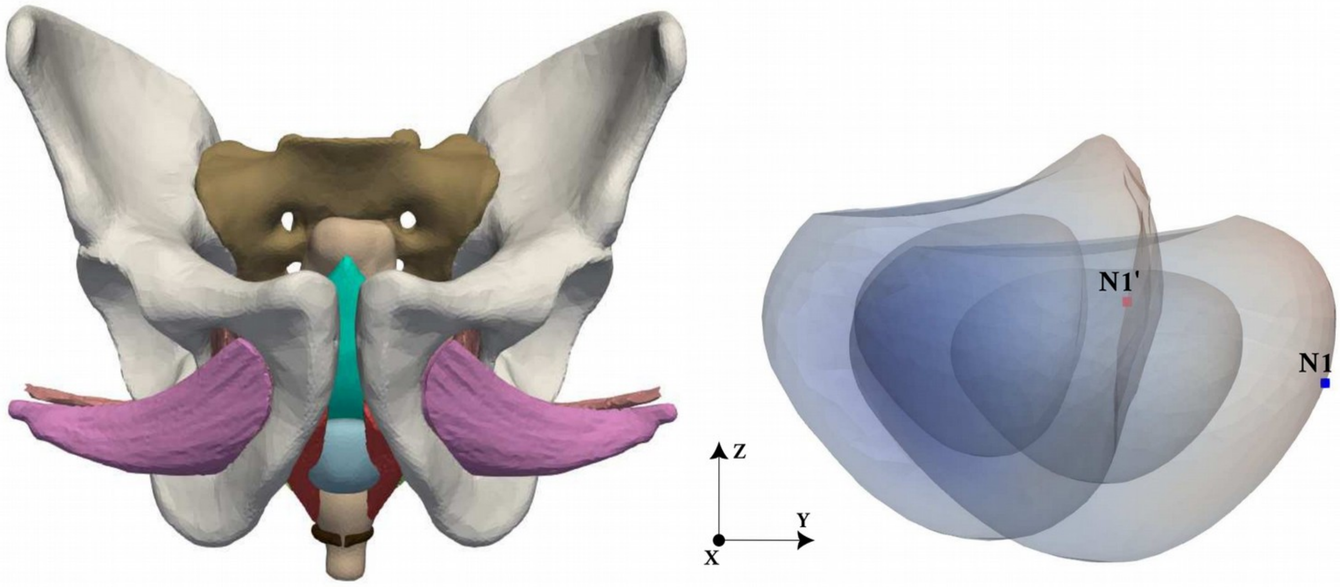

DOCTORAL THESIS
2022

Universitat Rovira i Virgili

Doctoral Thesis

Constitutive modeling of the male pelvic system to improve the accuracy of the location of neoplasms in MRI–TRUS fusion prostate biopsy

---

Author:
Muhammad Qasim

Supervisors:
Prof. Carme Olivé Farré
Dr. Gerard Fortuny

Departament d'Enginyeria Informàtica i Matemàtiques

August 30, 2022

UNIVERSITAT ROVIRA i VIRGILI

FAIG CONSTAR que aquest treball, titulat “Constitutive modeling of the male pelvic system to improve the accuracy of the location of neoplasms in MRI-TRUS fusion prostate biopsy”, que presenta Muhammad Qasim per a l’obtenció del títol de Doctor, ha estat realitzat sota la meva direcció al Departament d'Enginyeria Informàtica i Matemàtiques d’aquesta universitat.

HAGO CONSTAR que el presente trabajo, titulado “Constitutive modeling of the male pelvic system to improve the accuracy of the location of neoplasms in MRI-TRUS fusion prostate biopsy”, que presenta Muhammad Qasim para la obtención del título de Doctor, ha sido realizado bajo mi dirección en el Departamento de Ingeniería Informática y Matemáticas de esta universidad.

I STATE that the present study, entitled “Constitutive modeling of the male pelvic system to improve the accuracy of the location of neoplasms in MRI-TRUS fusion prostate biopsy”, presented by Muhammad Qasim for the award of the degree of Doctor, has been carried out under my supervision at the Department of Computer Engineering and Mathematics of this university.

Tarragona, 15 de Juliol de 2022

El/s director/s de la tesi doctoral
El/los director/es de la tesis doctoral
Doctoral Thesis Supervisor/s

Dra. Carme Olivé Farré

Dr. Gerard Fortuny Anguera

The research presented in this thesis was carried out with funding from the European Union's Horizon 2020 research and innovation programme under the Marie Skłodowska-Curie grant agreement 713679 and from the Universitat Rovira i Virgili (URV) under Grant 2018PFR-URV-B2-29.

UNIVERSITAT ROVIRA I VIRGILI

Abstract

Departament d’Enginyeria Informàtica i Matemàtiques

Doctor of Philosophy

Constitutive modeling of the male pelvic system to improve the accuracy of the location of neoplasms in MRI–TRUS fusion prostate biopsy

by Muhammad QASIM

Computational modeling of human pelvis using finite element (FE) method has become extremely important to understand the mechanics of prostate motion and deformation when transrectal ultrasound (TRUS) guided biopsy is performed. The number of reliable and validated constitutive FE models of the male pelvis region is limited, and given models did not precisely describe the anatomical behavior of pelvis organs, mainly of the prostate and its neoplasms location.

Prostate lesions are visible in Magnetic Resource Imaging (MRI) but it is difficult for radiologists to locate them at the time of performing transrectal ultrasound (TRUS) guided biopsy. Consequently, multiple biopsy samples are required to target one single lesion. The three-dimensional (3-D) anatomy model of the pelvic region (comprised of the rectum, bladder, pelvic muscles, prostate transitional zone (TZ), and peripheral zone (PZ)), based on medical images, is constructed and used for the simulations.

In this work, a new methodology is developed to help predict the location of neoplasms during the prostate biopsy. We investigated the biomechanical pelvis model simulations induced by soft tissue’s linear and non–linear material properties. More specifically, we targeted the relocation of five prostate lesions when the TRUS probe exerted a force at the inside rectum wall. The superimposed projections of slices are provided to target the lesions with a reasonable degree of accuracy. `Code_Aster` open source software is used for all the finite element (FE) numerical simulations. Moreover, we also developed a new constitutive model for anisotropic–viscoelastic behavior of the human prostate. The

new model is the independence of anisotropic and viscoelastic parts which are based on polynomial functions of certain invariants.

Our 3–D pelvis model simulations show that pressure exerted by the TRUS probe leads to two impacts on the prostate; motion and deformation. The prostate deformation and neoplasms displacement in between the linear and non-linear models showed that the varying material properties to organs altered the resulting lesion's migration parametrically. The distance traveled by the lesions in the linear elastic model ranged between 5.20 and 13.93 mm compared to those between 5.35 and 11.12 mm in the hyperelastic model. The PI-RAIDS (Prostate Imaging–Reporting and Data System) map and superimposition of slices using the registration technique provided an extra layer of information about prostate neoplasms location. However, additional research is required to validate our findings.

Our new constitutive model for anisotropic–viscoelastic behavior reproduces the probing (indentation) test data for prostate geometry in the corresponding FE numerical simulation. Furthermore, the invariants of the new model are the polynomial functions, which can provide a good fit to data where the linear and exponential functions of the invariants do not.

Resum

El modelatge computacional de la pelvis humana mitjançant el mètode d'elements finits (FE) ha esdevingut extremadament important per entendre la mecànica del moviment i la deformació de la pròstata quan es realitza una biòpsia guiada per ecografia transrectal (TRUS). El nombre de models FE constitutius fiables i validats de la regió de la pelvis masculina és limitat, i els models donats no descriuen amb precisió el comportament anatòmic dels òrgans de la pelvis, principalment de la pròstata i la seva localització de les neoplàsies.

Les lesions de pròstata són visibles a la imatge de recursos magnètics (MRI), però és difícil per als radiòlegs localitzar-les en el moment de realitzar una biòpsia guiada per ecografia transrectal (TRUS). En conseqüència, es necessiten múltiples mostres de biòpsia per orientar una única lesió. Es construeix i s'utilitza el model d'anatomia tridimensional (3-D) de la regió pèlvica (composat pel recte, la bufeta, els músculs pèlvics, la zona de transició de la pròstata (TZ) i la zona perifèrica (PZ)), basat en imatges mèdiques. per a les simulacions.

En aquest treball, es desenvolupa una nova metodologia per ajudar a predir la localització de les neoplàsies durant la biòpsia de pròstata. Hem investigat les simulacions del model biomecànic de pelvis induïdes per les propietats del material lineal i no lineal dels teixits tous. Més concretament, ens vam dirigir a la reubicació de cinc lesions de pròstata quan la sonda TRUS va exercir una força a la paret interior del recte. Les projeccions superposades de rodanxes es proporcionen per orientar les lesions amb un grau raonable de precisió. El programari de codi obert `Code_Aster` s'utilitza per a totes les simulacions numèriques d'elements finits (FE). A més, també hem desenvolupat un nou model constitutiu per al comportament anisotròpic-viscoelàstic de la pròstata humana. El nou model és la independència de les parts anisòtropes i viscoelàstiques que es basen en funcions polinomials de certs invariants.

Les nostres simulacions del model de pelvis 3D mostren que la pressió exercida per la sonda TRUS provoca dos impactes a la pròstata; moviment i deformació. La deformació de la pròstata i el desplaçament de les neoplàsies entre els models lineals i no lineals van mostrar que les propietats materials variables als òrgans alteraven paramètricament la migració de la lesió resultant. La distància recorreguda per les lesions en el model elàstic

lineal oscil·lava entre 5,20 i 13,93 mm en comparació amb les entre 5,35 i 11,12 mm en el model hiperelàstic. El mapa PI-RAIDS (Prostate Imaging-Reporting and Data System) i la superposició de rodanxes mitjançant la tècnica de registre van proporcionar una capa addicional d'informació sobre la ubicació de les neoplàsies de pròstata. No obstant això, es requereix investigació addicional per validar les nostres troballes.

El nostre nou model constitutiu per al comportament anisotròpic-viscoelàstic reprodueix les dades de la prova de sondeig (sagnia) per a la geometria de la pròstata en la simulació numèrica FE corresponent. A més, els invariants del nou model són les funcions polinomials, que poden proporcionar un bon ajust a les dades on les funcions lineals i exponencials dels invariants no ho fan.

Resumen

El modelado computacional de la pelvis humana utilizando el método de elementos finitos (FE) se ha vuelto extremadamente importante para comprender la mecánica del movimiento y la deformación de la próstata cuando se realiza una biopsia guiada por ultrasonido transrectal (TRUS). El número de modelos FE constitutivos confiables y validados de la región de la pelvis masculina es limitado, y los modelos dados no describían con precisión el comportamiento anatómico de los órganos de la pelvis, principalmente de la próstata y la ubicación de sus neoplasias.

Las lesiones de próstata son visibles en imágenes de recursos magnéticos (MRI), pero es difícil para los radiólogos localizarlas en el momento de realizar una biopsia guiada por ultrasonido transrectal (TRUS). En consecuencia, se requieren múltiples muestras de biopsia para apuntar a una sola lesión. El modelo anatómico tridimensional (3-D) de la región pélvica (compuesto por el recto, la vejiga, los músculos pélvicos, la zona de transición de la próstata (TZ) y la zona periférica (PZ)), basado en imágenes médicas, se construye y utiliza para las simulaciones.

En este trabajo se desarrolla una nueva metodología para ayudar a predecir la localización de neoplasias durante la biopsia de próstata. Investigamos las simulaciones del modelo de pelvis biomecánica inducidas por las propiedades del material lineal y no lineal del tejido blando. Más específicamente, nos enfocamos en la reubicación de cinco lesiones prostáticas cuando la sonda TRUS ejerció una fuerza en la pared interior del recto. Las proyecciones superpuestas de cortes se proporcionan para apuntar a las lesiones con un grado razonable de precisión. El software de código abierto `Code_Aster` se utiliza para todas las simulaciones numéricas de elementos finitos (FE). Además, también desarrollamos un nuevo modelo constitutivo para el comportamiento anisotrópico–viscoelástico de la próstata humana. El nuevo modelo es la independencia de partes anisotrópicas y viscoelásticas que se basan en funciones polinómicas de ciertos invariantes.

Nuestras simulaciones de modelos de pelvis en 3-D muestran que la presión ejercida por la sonda TRUS conduce a dos impactos en la próstata; movimiento y deformación. La deformación de la próstata y el desplazamiento de las neoplasias entre los modelos lineales y no lineales mostraron que las diferentes propiedades del material en los órganos alteraron paramétricamente la migración de la lesión resultante. La distancia recorrida

por las lesiones en el modelo elástico lineal osciló entre 5,20 y 13,93 mm frente a los 5,35 y 11,12 mm en el modelo hiperelástico. El mapa PI-RAIDS (Prostate Imaging-Reporting and Data System) y la superposición de cortes utilizando la técnica de registro proporcionaron una capa adicional de información sobre la ubicación de las neoplasias prostáticas. Sin embargo, se requiere investigación adicional para validar nuestros hallazgos.

Nuestro nuevo modelo constitutivo para el comportamiento anisotrópico–viscoelástico reproduce los datos de prueba de sondeo (sangría) para la geometría de la próstata en la simulación numérica FE correspondiente. Además, las invariantes del nuevo modelo son las funciones polinómicas, que pueden proporcionar un buen ajuste a los datos donde las funciones lineales y exponenciales de las invariantes no lo hacen.

Acknowledgements

I would like to express my gratitude to Martí i Franquès COFUND fellowship at Rovira i Virgilli (URV) University for their financial support. It has been an honor to be a part of URV and I am grateful for providing complete academic freedom in this research.

I am grateful to my supervisors, Dr. Olivé Farré, Dr. Gerard Fortuny, Dr. Dolors Puigjaner, Dr. Josep M. López, and Dr. Joan Herrero. Thank you all for giving me an opportunity to join your group and for your time, especially during my first year of PhD studies. Those regular meetings helped me a lot to polish my skills in the field of Biomechanics. I want to thank everyone for their patience when the results were not favorable and feedback after the discussions and the presentations. And of course, for your time reading and correcting my manuscripts. Completing this project in collaboration with you was a refreshing experience, especially related to our new anisotropic–viscoelastic constitutive model.

Dr. Gerard, thank you very much for your assistance with the study and paperwork and for your time reading my emails and messages on WhatsApp, even though it was the weekend or night. I appreciate your unwavering optimism. Dr. Joan and Dr. Joseph, you are my Cum Laude supervisors! You were always nice and friendly, Dr. Dolors, one of the project module leaders. I appreciate your encouragement and support throughout the research work. A profound sense of gratitude to the pathfinder of this research project, Dr. Carme Olive, who has always been a key person for me and made it possible to work with the group members.

I had the wonderful opportunity to spend three months at the NTNU university in Trondheim, Norway. A special 'thank you' goes to Dr. Victorian E. Prot for the encouragement and introducing me to the world of the anisotropic-viscoelastic constitutive model.

Thanks to the COFUND and human resource teams, Dr. Oana, Paloma, Anna and Sandra. You were accommodating for all the administration work especially getting the resolution letter every year from the ministry. My sincere gratitude to all my friends from this university and home; we have had friendly and encouraging talks. My university mates, Najeeb, Jaffar, Faiz and Elen, we have had very good cooperation. I appreciate your moral assistance as well. Also, I would like to thank my homeland friends, Saddam, Shoaib and Muneer, for their continuous support and for keeping me motivated.

I cordially thank my parents and siblings for the constant love, affection, moral support and prayers. Your prayers for me were what sustained me this far. My wife deserves a special thanks for her continuous support and understanding of my research life. I appreciate you being my second half. Also, lots of love for my daughter for her cute smiles and daily fun, which help to lift my spirits.

Above all, praises and thanks to Allah Almighty for the showers of blessings throughout my life and for giving me strength and courage to in the times of problems and despair.

Contents

List of Figures

List of Tables

List of Abbreviations

3–D	**T**hree dimentional
AI	**A**rtificial intelligence
CT	**C**omputerized tomography
FE	**F**inite element
MRI	**M**agnetic resonance imaging
PCa	**P**rostate cancer
PZ	**P**rostate peripheral zone
SMM	**S**tatistical motion models
TRUS	**T**ransrectal ultrasound
TZ	**P**rostate transitional zone
PI-RAIDS	**P**rostate Imaging-Reporting and Data System
GLOBOCAN	**G**lobal cancer observatory
PSA	**P**rostate specific antigen
DRE	**D**igital rectal examination
PFMs	**P**elvic floor muscles
MP	**M**ulti parameter
BPH	**B**enign prostate hyperplasia
PSAD	**P**SA density
TP	**T**ransperineal biopsy
TR	**T**ransrectal biopsy
AFS	**A**nterior fibromuscular stroma
COM	**C**enter of mass
E	**E**lastic modulus
SEF	**S**train energy function
C	**C**auchy green tensor
F	**D**eformation gradient

J	**D**eterminent
S	**S**econd Piola–Kirchfoff stress tensor
$\overline{\mathbf{C}}$	**M**odified Cauchy–Green tensor
K	**B**ulk modulus
MPa	**M**ega pascals
KVFD	**K**elvin–Voigt fractional derivative
DOF	**D**egree of freedom

To my parents, my brothers, my sisters, my wife and my daughter

Chapter 1

Introduction

This chapter highlights the details about the general context of the methodology and provides the background work related prostate cancer, MRI/TRUS fusion registration methods, constitutional models and explains the objectives of this thesis. Additionally, it displays the thesis organization and the published and in–progress papers as an index of its scientific quality.

1.1 Introduction

The structure of the male pelvis is an inter–related system of rectum, bladder, prostate, pelvic floor muscles, and bony pelvis with multiple functions. Therefore, it is essential to know the theoretical and practical knowledge of male pelvis anatomy when dealing with prostate cancer problems. One such study showed that men are less aware of basic male anatomical ideas, like in the relationship between prostate with urethra and rectum; only 32% and 25% are aware of anatomy concepts [106].

The prostate is located in the center, anterior to the rectum and inferior to the bladder. The pelvic floor muscles beneath the prostate also support the prostate, as shown in Fig. 2.1 [102, 79]. The prostate is divided into four histological zones; the transition zone, peripheral zone, central zone and the anterior fibromuscular stroma. About 70–75 % of prostate cancer (PCa) typically arises in the peripheral zone of the gland near the rectum wall and 20–30 % in the TZ [112].

Transrectal ultrasound (TRUS) biopsies are commonly used in clinical practice for decades. It involves an ultrasound probe into the rectum to target the tissue samples. Physicians also commonly use another method, the transperineal approach; a biopsy needle passes through the perineum instead of the rectum. Both approaches have pros and cons, but overall, PCa detection rates are similar between the transrectal and transperineal approaches [77, 120, 122].

Magnetic resonance imaging (MRI) has become increasingly popular in recent years to provide the contrast between normal tissue and prostate lesions. Studies have shown that the MRI-targeted biopsy method increases the overall and clinically meaningful PCa detection rate. Additionally, it significantly lowers the detection rate of prostate tumors that are not clinically significant, avoiding overtreatment [4, 44, 35]. But the lengthy scanning process and high expenses have limited its usage in prostate biopsy. Therefore, the fusion of MRI and TRUS images has been developed to guide prostate biopsies, providing more information to reduce the false-negative prostate cancer diagnosis [83, 98]. The MRI-TRUS fusion technologies rely on the registration process, which involves superimposing the MRI image set with the appropriate real-time TRUS images, producing low-cost and high-resolution images [117, 40].

The main difference between MRI/TRUS fusion registration for prostate biopsy is the image registration method, which is either rigid or elastic. The first method involves co-registration of MRI images onto the TRUS images after paired landmarks are established in both. The second method, elastic registration, deform the MRI image according to the deformation caused by the introduction of the TRUS probe [25]. In comparison to TRUS alone, both rigid and elastic methods significantly reduced the number of false-negative outcomes, 14% [105] and 31.4% [84], respectively.

However, only elastic registration considers the pressure of TRUS probe at the rectum wall, which causes prostate motion and deformation. According to Xu and Penzkofer et al. [121, 80], both rigid and elastic deformation have reported biopsy accuracy to be under 3 mm. In a study using a phantom model [43], there were no significant differences between rigid and elastic registration errors (4.11 vs. 4.87 mm, p=0.05). In fact, according to Hale et al. [29], although a slightly higher cancer detection rate has been reported with elastic compared to rigid registration.

Moreover, identifying the mechanical properties of pelvis organs is important to understand the anatomical behavior of organs/tissue-organs, as evidenced by the variety of experimental research [20, 67, 54, 64, 55]. These properties serve as a basis to assess tissues' remodeling process and execute computer simulations of surgical interventions and medical device applications. A constitutive model often specifies the relation between the stresses to which a material is subjected and the strain response. The response is mostly determined by the material's underlying constituents and their mechanical behavior.

This thesis aims to obtain a universal model of pelvis organs that predicts the prostate motion, deformations, and neoplasms final location when the TRUS probe applied the force of 30 N at the rectum wall. Therefore, our first step is to simulate the biomechanical model with the linear properties of tissues/organs. The second step is to apply the non-linear material properties to the organs derived from experimental stress-strain data based on tissue testing in the articles. In the third step, we provide the new constitutive model for anisotropic-viscoelastic behavior of the prostate.

1.2 Background

Cancer has emerged as a leading cause of death and Prostate Cancer (PCa) is the tumor with the highest incidence and mortality rate from cancer in men in the world and third in the EU [13, 38]. Global cancer observatory (GLOBOCAN) 2018 estimated 1.3 millions new cancer cases and almost 359,000 deaths were caused by PCa worldwide, which increased to approximately 14.84% and 2.85% registered cases and PCa deaths in 2020, respectively [13, 111, 108].

The most common methods used in PCa diagnosis are the Prostate Specific Antigen (PSA) test and the Digital Rectal Examination (DRE) test [30]. The PSA test is a blood test that determines the amount of KLK3 glycoprotein enzyme, an enzyme which is produced by prostate cells, present in blood [92, 10, 86]. In the DRE test, which is the least invasive diagnosis procedure, the practitioner inserts a gloved, lubricated finger into the rectum to palpate the prostate for anything abnormal [74, 75]. Nowadays, transrectal biopsy is used to diagnose the prostate cancer when serum PSA is abnormal [11]. If prostate cancer is suspected, as is the case when values of PSA value in the range of 3.0–9.9 μg/L are obtained, a transrectal ultrasound (TRUS) scan is usually performed [39]. TRUS allows radiologists to determine the prostate's size, shape and glandular structure [104].

Cancerous prostate tissue is stiffer than benign and normal one [58, 82]. However, manual palpation of cancerous lesions can be difficult when the elastic properties of unhealthy tissue are similar to those of healthy one [15]. Furthermore, in a DRE test, it is quite difficult to provide any statistical or numerical information; therefore, its effectiveness depends on the skills and expertise of the physician [115]. In transrectal ultrasound

(TRUS) guided biopsy, it consists of inserting a needle through the rectum wall and towards the prostate to obtain a sample of potentially cancerous tissues. The procedure is conducted using ultrasound images that are obtained by an endorectal probe [60].

The motion and deformation of the prostate during TRUS–guided biopsy make it difficult to know the location of potential lesions in advance. Therefore, when using this procedure, practitioners can only provide rough estimations for the locations of the lesions. Consequently, multiple biopsy samples are required to target one single lesion [97]. However, an increase in the number of biopsy samples can augment undesirable associated complications such as rectal bleeding, hematospermia (blood in semen), hematuria (blood in urine), and infections [1]. Wang et al. [116] proposed the combined statistical and biomechanical methods to investigate the prostate deformation under different ultrasound probe insertion conditions. In particular, Wang et al. [116] provided patient specific biomechanical parameters, acquired from ultrasound elastography, for the inner and the outer prostate for a data set with twelve patients.

Other authors used finite element (FE) based statistical motion models (SMM) on estimating the shape adopted by a prostate when it was deformed because of TRUS probe pressure [51, 72]. Baratha et al. [7] proposed a deformable image registration system based on a biomechanical 3-D FE modeling with linear elastic properties for the prostate. Marchal et al. [66] implemented a discrete modeling method to simulate the prostate's displacement and deformation due to internal interactions between organs and external interactions between organs and surgical tools, such as the needle. Other studies [56, 12], performed in the context of prostate radiotherapy, also provide interesting information on how to address the challenging problem of motion and deformation of the prostate.

In the last few years, there has been a tendency to include information from magnetic resonance images (MRI) to guide prostate biopsy. In parallel, several commercial platforms for guided biopsies have been launched into the market [28]. According to Warlick et al. [117], guided biopsy platforms that include MRI images can be classified into the following three categories: MRI-compatible prostate biopsy systems, MRI-TRUS fusion biopsy systems and Robotic in-bore MRI biopsy systems. However, the integration of several different technologies and devices into a platform is a costly process. Consequently, acquiring one of these commercial guided biopsy platforms is not affordable for all healthcare providers.

Studying human injuries and associated prevention methods heavily relies on the mechanical properties of soft tissues. Such properties are crucial for the computational modeling of biological systems [100]. Pathologists are medical professionals who examine bodies and tissues. Sometimes it is hard for them to collect every type of human tissue to meet the specific needs of investigators [41]. Due to the slow rate of human studies, tissues are not routinely accessible for research, as interventional trials are few and far between [41]. The investigators moved to their alternative way i.e. on animals tissues mostly pig's; rectum and bladder [89, 57, 16], rat bladder [27] and monkey ligaments [114] are mostly used as an experimental subjects.

However, some experimental data on humans meet the anatomical behavior of male pelvis organs. For example, human prostate and rectum mechanical behavior were examined at different morphologies under various loading speeds [55, 68, 33]. The complex and dynamic nature of PFMs between ligaments and fascias that are connected to the pelvic bones provide strong support to the pelvic organs [94]. Janda et al. [54] investigated the uniaxial and biaxial loading on pelvic floor muscles (PFMs) and provided the non-linear passive properties. A similar uniaxial tensile test was performed on a human female bladder [67]. The periurethral tissues were obtained from the whole ex-vivo prostate and mechanical behavior was modeled [64].

The comparative studies of human and animal tissues (rectum and bladder) revealed the tensile properties are different and non-identical in between each organ [22, 27]. Even the mechanical behavior of old and young women's tissues (rectum, bladder, ligament and the vagina) divulged the anisotropic behavior between the organs [93, 20]. Johnson et al. [55] evaluated the similar and distinct mechanical response of human and porcine prostate glands using probing and compression testing methods.

A good attempt has been made to develop 3–D FE pelvis model as an integrated system comprising of muscles, ligaments and bony pelvis to investigate the mechanical behavior of female pelvic floor dysfunctions [8]. However, no attempt is being made to develop a universal model that can incorporate in-vivo mechanics such as the effect of TRUS beam pressure on the rectum wall, prostate and other pelvic organ deformations. Despite the fact that several methodologies have been proposed in the past [12, 66, 65], reliable material coefficient and valuable constitutive expressions to incorporate in the analysis are still lacking.

1.3 Goal of the Thesis

This thesis presents an alternative methodology that can improve the location accuracy of prostate neoplasms during MRI–TRUS fusion biopsy. Moreover, a new constitutive model helps to analyze the anisotropic–viscoelastic behavior of prostate. The main research goals of this thesis are:

- To integrate an accurate and realistic 3–D geometry of the pelvic region.
- To obtain the biomechanical simulation of pelvis organ taking into consideration the tissues′ homogeneous and isotropic linear elastic properties.
- To obtain the non–linear material properties by remodeling the mechanical loading data in the literature.
- To use this non–linear material properties into a computational finite element (FE) model for biomechanical analyses of pelvis organs.
- To use the linear and non–linear FE models to simulate the prostate's biomechanical response and actual location of prostate neoplasms when the pressure is applied by the TRUS probe on the rectum wall during a TRUS–guided biopsy.
- To observe, compare and analyze the pelvis organ deformation, lesions displacement of prostate and with using the co-registration technique between linear and non–linear FE models results.
- To obtain the new constitutive model for anisotropic–viscoelastic behavior of the prostate to improve the understanding of prostate mechanics.

1.4 Thesis Structure

The thesis is outlined as follows:

The second Chapter explains the anatomy of the pelvis model and the location where TRUS pressure is applied at the rectum wall. We propose a new methodology that predicts the final location of the prostate lesion during a TRUS biopsy. For this, we apply linear elastic material properties to the tissues to mechanically characterize the behavior of pelvis organ mainly of the prostate and its lesions location. Additionally, we provide the MRI–TRUS fusion registration technique that gives an extra layer of knowledge to target the prostate neoplasms correctly when performing a biopsy. Moreover, we also provide the PI-RAIDS maps with the approximate situation of five selected nodes on the prostate for the feasibility of the surgeons targeting the lesions with a reasonable degree of accuracy.

In Chapter 3, we propose an isotropic hyperelastic approach to most soft tissues except vesical muscles, which are assumed to have a linear elastic behavior. First, we display the material coefficients of soft tissues except vesical muscles obtained by remodeling the existing mechanical data under different probing techniques mentioned in the literature. Next, we assume the linear elastic properties of vesical muscles due to the lack of experimental data. Then we obtain the deformation of pelvis model using linear and non-linear material properties by applying the TRUS probe force at the rectum wall. In the end, we compare pelvis organ deformation, lesions displacement and co-registration image technique with the results obtained in Chapter 2.

Chapter 4 begins with implementing a new constitutive model for anisotropic viscoelastic behavior of prostate at strain rate 25% and is implemented in open-source finite element software `Code_Aster` coupling with `MFront` code. The codes are provided in the appendix section of this thesis.

Finally, Chapter 5 concludes the remarks regarding the objectives of this thesis and the author explains some future research related to this research work.

1.5 Publication List

Some of the results presented in this thesis are from the following published/in–progress articles.

1. **Qasim M**, Puigjaner D, Herrero J, López JM, Olivé C, Fortuny G, Garcia-Bennett J. Biomechanical modelling of the pelvic system: improving the accuracy of the location of neoplasms in MRI-TRUS fusion prostate biopsy. BMC cancer. 2022 Dec; 22(1) : 1-0.

2. **Qasim M**, Puigjaner D, Herrero J, López JM, Olivé C, Fortuny G, Garcia-Bennett J. Hyperelastic constitutive modeling of the male pelvic system to understand the

prostate motion, deformation and neoplasms location with the influence of MRI-TRUS fusion biopsy. IEEE. Transaction on Biomedical Engineering (To be submitted).

3. **Qasim M**, Puigjaner D, Herrero J, López JM, Olivé C, Fortuny G, Garcia-Bennett J. A new constitutive model for anisotropic–viscoelastic behavior of human prostate. Journal of the Mechanics and Physics of Solids (In–progress).

Chapter 2

Linear Elastic Model

Knowledge about the motion of pelvis organs is of great importance to predict the location of prostate lesions during prostate biopsy and to prevent mispositioning during the treatment session. Moreover, prostate lesions are visible during Magnetic Resource Imaging (MRI) scanning. However, it is difficult for the radiologist to locate them when performing a TRUS-guided biopsy. This chapter explains the three–dimensional (3-D) anatomy model of the pelvic region, which we will use for simulation results. In addition, this chapter presents the new methodology to target the final location of prostate lesions when TRUS probe pressure is applied. The work aims to reduce the number of prostate biopsies.

2.1 Introduction

Transrectal ultrasound (TRUS) guided prostate is used to achieve a histopathological diagnosis of prostate cancer and has been standard procedure in urology for about thirty years [71]. In 1937, Astraldi was the one who described the first transrectal biopsy of prostate [6]. Later on, it was applied by Takahashi and Ouchi in 1964, and Watanabe and colleagues enhanced it in 1967 [107], according to Moe et al. [71].

Xiang et al. [120] described the comparison between transperineal (TP) biopsy and transrectal (TR) biopsy and concluded that both have the same diagnosis accuracy, but TP prostate biopsy is safer and more valuable because of lower risk of infection and rectal bleeding. Other authors' concerns about the serious complications during the biopsy such as rectal bleeding, sepsis, hematuria, fever, and acute urinary retention [85, 95, 122, 81, 42]. Even though many studies were conducted to assess the detection rate and complication between TP and TR prostate biopsy techniques, the results remained controversial [37, 31, 2].

This chapter describes the deformation of pelvis model when TRUS beam pressure applied at the rectum wall. More importantly, it discusses the prostate neoplasms location when prostate motion and deformation occur. Also, the use of PI-RAIDS maps and superimposition of slices using the registration technique provides extra layer of knowledge to target the prostate neoplasms location.

2.2 Geometric Model

The complex geometry of the male pelvis using the finite element (FE) method is essential for biomechanical analysis and computer convergence. We obtained our pelvis model from body-parts 3-D [70]. This dictionary-type anatomical database contains 3-D triangular surface models defining the corresponding individual elements like bones, muscles, and organs. These 3-D surface meshes are conveniently modified to solve consistency and integrity problems using homemade and open source software [17]. Then the set of 3-D meshes was uploaded into the Gmsh open-source software [36] where 3D tetrahedral volume meshes were obtained using the Netgen algorithm. So, the organs and soft tissues were assembled into a single model according to the male pelvis anatomy. A total number of 180,766 triangles and 655,355 tetrahedra were used in the pelvis model. The final anatomical model used is shown in Figure 2.1 is well adapted for mapping pelvis organs anatomy into a finite element model for biomechanical analysis. The model demonstrated for pelvis organs is comprised of pelvic bones (hip and sacrum bones), pelvic muscles (obturator internus, obturator externus, iliococcygeus, pubococcygeus, puborectalis, and vesical muscles), anus, rectum, bladder and the prostate transitional zone (TZ) and peripheral zone (PZ).

From an anatomical point of view, the prostate is a dense fibromuscular gland and is located at the center and lower part of the pelvis, just beneath the bladder where they contact. Anteriorly, it is posterior to the hip bones, and posteriorly it is anterior to the rectum and plays a supportive role in the male reproductive system [12, 101]. The puborectalis and pubococcygeus muscles of the levator ani muscle, coupled with other pelvic floor muscles, also provide primary support to the prostate, as does the urogenital diaphragm (see Figure 2.1).

The prostate consists of three parts; the base (only part of the prostate where the prostate and bladder intersect), the mid gland, and the apex (inferior part). Histologically, the prostate gland is composed of different zones as described in PI-RADS (Prostate Imaging-Reporting and Data System)[112]. Based on these zones mentioned in Fig. 2.2, the gland is divided into four anatomical zones; the peripheral zone (PZ), the central zone (CZ), the transition zone (TZ), and the anterior fibromuscular stroma (AFS).

2.3 Material and Methods

In this section we assume that the relation between stress-strain for isotropic material is linear. The generalized Hook's law is written as the linear relationship between stress and strain as:

$$\boldsymbol{\sigma} = \mathbf{E} : \boldsymbol{\epsilon} \tag{2.1}$$

where stress $\boldsymbol{\sigma} = \sigma_{ij}$, strain $\boldsymbol{\epsilon} = \epsilon_{kl}$ is a rank 2 tensors, and $\boldsymbol{C} = C_{ijkl}$ is a rank-4 tensor. Consider the relationship between stress and strain of a ductile material in Fig. 2.3. According to this behavior, the relative deformation of the material (strain) is proportional to the force per unit area (stress) applied to it. For linear elastic behavior, two parameters are needed: Young's modulus, E, which measures the stiffness of the material (technically, E is the ratio between stress and strain i.e., $\frac{\Delta\sigma}{\Delta\epsilon}$, so that the larger E, the stiffer the material) and the Poisson's ratio, η, which measures the relative volume change [53]. The yield point in Fig. 2.3 illustrates that the material leaves the elastic region, and after that, it suffers permanent deformation. The ultimate strength is the maximum stress that a material can resist, and the fracture point is where the material breaks.

We tried to produce the results as closely as possible to a TRUS-guided biopsy's real-world conditions in our simulations. In clinical practice, the TRUS guided biopsy is used to target prostate lesions by applying pressure on one side of the rectum [123]. Because a U-shaped puborectalis muscle forms a strong sling that pulls the anorectal junction of the pubis from anteriorly to the posterior. The resulting effect makes an anorectal angle between the anal canal and rectum [96], using probe in this way finds the path of less resistance and reduced pain.

A similar angled area of the rectum wall is being used to apply the pressure of the TRUS probe to the inner rectum wall. Therefore, we hypothesized that a 30 N force was applied orthogonally to a 258 mm^2 surface patch of the rectum wall as shown in Fig. 2.1 whereas the force is an estimation of the one applied by the practitioner during TRUS over the surface patch of the rectum wall. The surface patch is the area that represents the average shape and size of the contact between the transducer (EC9-4 Siemens Acuson sidefire endocavitary probe) and the rectum wall.

The boundary conditions greatly affect the mechanical behavior of the computational model. For the sacrum and hip bones, kinematics boundary conditions were assumed, i.e., zero deformation boundary conditions. The numerical simulations were done in `Code_Aster` open-source FE software [36] to study the linear elastic behavior of our model. Linear material models are usually preferred because they provide faster results compared to non-linear material model and the main limitations of the linear models are they cannot accurately predict large deformations [72].

The biomechanical parameters of the prostate and around elements vary among individuals, and they are different for each aspect of the same subject [116, 26]. The Young's modulus for the TZ and PZ tissue in this study was chosen from Wang et al. [116] patient's case 6, which was acquired via shear wave elastography. The Poisson ratio (η) for prostate tissues was fixed to 0.495, as recommended by Krouskop et al. [58]. Other organ material properties (Young modulus and Poisson's ratio) were taken from the literatures [59, 22, 46, 14, 90, 19], and their specific values are reported in Table 2.1. The deformation and stress fields are the major outputs of a FE simulation, and the computed deformation field was the subject of this research work.

We selected five mesh nodes in the original geometry at different locations in coronal, sagittal, and axial planes as indicated in Fig. 2.4. Thus, the nodes N1, N3, N4, and N5 are chosen for the peripheral zone of the prostate, while the node N2 is selected for the Prostate transitional zone. The displacement of these nodes was tracked by measuring their consequent location in the deformed geometry.

2.3.1 Results

The complete anatomy of the pelvis organs accomplishes the boundary conditions and provides realistic support for the prostate deformations, enhancing the effectiveness of biopsy manipulation. Figure 2.6 shows the simulation results of prostate, rectum, and bladder organs movement, taking into account the different conditions mentioned above. According to the simulation, a TRUS beam pressure of 30 Newton (N) at the inside rectum wall close to the prostate leads to substantial movements in the prostate transitional and peripheral zones. As a result, the prostate deformed towards the ventral region.

The anterior part of the rectum showed the maximum displacements (see Fig. 2.5) of around 19 mm in the Y direction, causing a significant displacement on the PZ and TZ contours, of approximately 15 mm and 12 mm respectively. At the same time, the bladder was almost 9 mm displaced cranially at the points where the prostate and bladder contact (Z direction). On the other hand, exactly zero displacements were seen on the sacrum and hip bones because of the stiff properties of the bones (see Fig. 2.5).

The displacements of small lesions in the prostate are given in Tab. 2.2 which exhibits the final position for each node. We also replicated the nodes on a PI-RAIDS maps [112, 3] shown in Fig. 2.2; nodes N1 and N4 are located near the outer surface of PZpm, N3, and N5 are located near the PZpl and AFS exterior surfaces, respectively, and the N2 node is within the TZ. The radiologists could use this information to find each node studied correctly when performing the biopsy using guided ultrasound. The size of displacements was calculated by the L_2 norm of displacement in X, Y, and Z directions for each selected node. According to Fig. 2.7, the node "N1" showed the highest displacement because it

Table 2.1: Material properties of the elements in our model for the pelvic region: Elastic modulus (E), Poisson's ratio (η) and density (ρ).

Organ	E(kPa)	η	ρ (kg/m^3)	Source
Prostate transitional zone	43	0.495	1500	[116]
Prostate peripheral zone	18	0.495	1500	[116]
Bladder	10	0.499	1500	[59]
Rectum	5180	0.499	1500	[22]
Anus	10	0.499	1500	[46, 19]
Obturator internus muscles	15	0.4	1500	[46, 19]
Obturator externus muscles	15	0.4	1500	[46, 19]
Iliococcygeous muscles	15	0.4	1500	[46, 19]
Pubococcygeous muscles	15	0.4	1500	[46, 19]
Puborectalis muscles	15	0.4	1500	[46, 19]
Vesical muscles	150	0.4	1000	[14]
Brock2006 Sacrum bones	11×10^6	0.26	1640	[90]
Hip bones	11×10^6	0.26	1640	[90]

lies nearby the rectum side. In contrast, the node "N3" has the lowest displacement due to the boundness of puborectalis and pubococcygeus muscles. The node "N5" opposite to "N1" has a displacement value of 5.51 mm, and also the nodes "N2" and "N4" have the displacement values of 8.26 mm and 6.78 mm, respectively.

To present the whole displacement of prostates, we also calculated the center of mass (COM), i.e. X = -0.66 m, Y = -82.30 m, Z = 782.49 m, to localize the specific location of a node with the help of using `Code Aster` via `Salome_Meca` software [36]. After the TRUS beam pressure simulation, the COM of that node displaced around -1.21 mm, 6.73 mm, and 2.45 mm in the X, Y, and Z directions, respectively.

The superimposed projection of original and deformed prostate geometry in the sagittal plane is shown in Fig. 2.7. This is due to the effect of TRUS probe pressure of 30N inside the rectum wall, which leads to two major impacts on the surface contours of the prostate; motion and deformations. In prostate motion, we have the displacement in an absolute frame of reference, whereas in deformation, we have the volume and shape change in the prostate gland. In Fig. 2.7, the shape of the original prostate resembles the surface of an idealized ellipsoid, whereas the deformed contour has a much more irregular shape.

Fig. 2.8 presents an axial slice with an N1 lesion with the same vertical location (Z = 0) as the lesions were observed in the original MRI image. However, after the rigid registration, considerable deformation is experienced by the prostate, which makes the final slice quite different from the original one. We have not depicted the real N1′ (displaced node) 3-D location but its projection in the axial and sagittal plane. As a result of deformation, our biomechanical model predicts a small leftover displacement of N1, which is consistent with the fact that the real human body will never be 100 % accurate.

When we look for the final N1′ location in the original (X=0) axial plane, the sagittal slices superimposed in Fig. 2.8(c) reveal that the main source of error is in the normal coordinate system (Z). The value of Z = 5.16 mm in Table 2.2 suggests that the ultimate N1′ location will be in that plane rather than the original axial location (Z = 0). This is accounted for in Fig. 2.8(b) when the proper slice (deformed slice is in own axis not at Z = 0) for N1′ is used for registration. The axial polar plots in Figures 2.8(a and b) are very similar. This key point will help the practitioner during registration that exactly where the small lesions need to be a target, as the estimation of X and Y coordinates of the lesions in the TRUS image would have been known. But as Fig. 2.8(c) clearly demonstrates, even with a precise projection of the lesion in the axial plane, there is still a chance that the axial position (Z) of the lesion might be estimated with a significant amount of inaccuracy.

Table 2.2: Coordinate displacements and their magnitudes of prostate lesions w.r.t. nodes after applying TRUS pressure at rectum wall

		Displacements (mm)			
Node	Location in prostate	DX	DY	DZ	Magnitude
N1	PZ midsaggital, intermediate level	0.94	-12.91	5.16	13.93
N2	TZ midsaggital, intermediate level	-0.66	-7.84	2.52	8.26
N3	PZ lateral, intermediate level	3.37	-4.56	1.70	5.20
N4	PZ midsaggital, apex level	0.68	-6.56	1.56	6.78
N5	PZ midsaggital anterior, intermediate level	0.34	-5.53	0.94	5.51

2.4 Discussions and Conclusions

The purpose of registration is to help the practitioner locate a tumor by removing or at least lowering one of the TRUS effects, prostate motion and deformation (see Fig. 2.7). To target a lesion with an acceptable degree of accuracy, the two superimposed slices from MRI and TRUS should show similar shapes of the prostate. Our computer calculations demonstrated that a 30 N TRUS probe force applied to the rectum wall resulted in significant deformation of prostate TZ and PZ.

In Fig. 2.8, the idea to represent the superimposed slices of the original and deformed prostate with the different location of node N1 was followed by Igarashi et al. [52]. It attempts to approximate the type of representation generated by an MRI-TRUS rigid registration technique when tracking the N1 node. Thus the polar coordinate framework's concept is to establish the polar system's origin in the original (undeformed) slice, the corresponding origin in the deformed slice, and then translate the deformed slice origin into the prior one (undeformed slice), resulting in the superimposition of both images.

Therefore, the biomechanical approach presented in this study provides an extra layer of knowledge that might significantly improve the accuracy of the MRI-TRUS fusion procedures. Moreover, our FE simulations in this study were limited to tracking small prostate lesions that could be assimilated to a node in the computational mesh. We believe that this present methodology could easily be extended to follow the deformation and displacement of large lesions. This can be done if we define the collection of volume elements for each neoplasm and assign a stiff elastic modulus (E) and η value because cancerous tissues are stiffer than benign and normal prostate tissues [58, 82, 50].

There are several limitations to our research. The biomechanical model did not incorporate the central zone that surrounds the ejaculatory ducts, which contains 20 % of the glandular tissue and anterior fibromuscular stroma (contains no glandular tissues) of the prostate [3]. However, these zones account for less than 25 % of the normal prostate volume, and only 10 % of neoplasms develop in these areas. Moreover, we did not consider the different prostate volumes, the prostate's transition zone, and how much bladder volume affects prostate motion and deformation. Some authors studied prostate effects with the volume contained in other pelvis organs. For example, Keros et al. [56] have reported prostate movements from changes in organ volume. The motion of the prostate has been empirically estimated by considering changes in rectal, bladder, and lung volumes. The interaction of the pelvic organs due to concomitant changes in organ volumes was also used for numerical results [12]. An approach was proposed to use a discrete modeling method to simulate the displacement of the prostate secondary to changes in bladder volumes, ultrasound probe pressure, needle insertion, and brachytherapy interventions [66]. However, it is quite difficult for us to include the volume of organs and compare the deformation values with other studies because of different methodologies.

The development of AI approaches based on deep neural networks is a new trend in the field of image registration [44, 52, 119, 21]. However, the design of robust techniques that generate the samples utilized in the network training stage is a critical challenge in those methodologies [44]. Furthermore, we believe that it is quite common to construct these samples by taking image pairs that have been manually recognized by medical specialists, with the consequence of significant expenditure of work and time. Therefore, we think our new methodology might also be utilized to create pairs of registered images that constitute robust training samples.

In this research work, we proposed an alternative strategy to register an image of MRI and ultrasound, considering the biomechanical properties of pelvic tissues like obturator internus and obturator externus iliococcygeus, pubococcygeus, puborectalis, and vesical muscles. We used finite element simulations to obtain the results of the pelvic region with the setting of an accurate and realistic 3-D geometric configuration. It provides information about the neoplasm and the effect of the TRUS beam on other pelvic organ deformations. This new methodology predicts the site of neoplasm during a biopsy, but it can significantly be improved if further studies find clinical settings to validate our findings. Furthermore, because our technique is entirely based on open-source software, its adoption would be reasonable for healthcare facilities with limited resources.

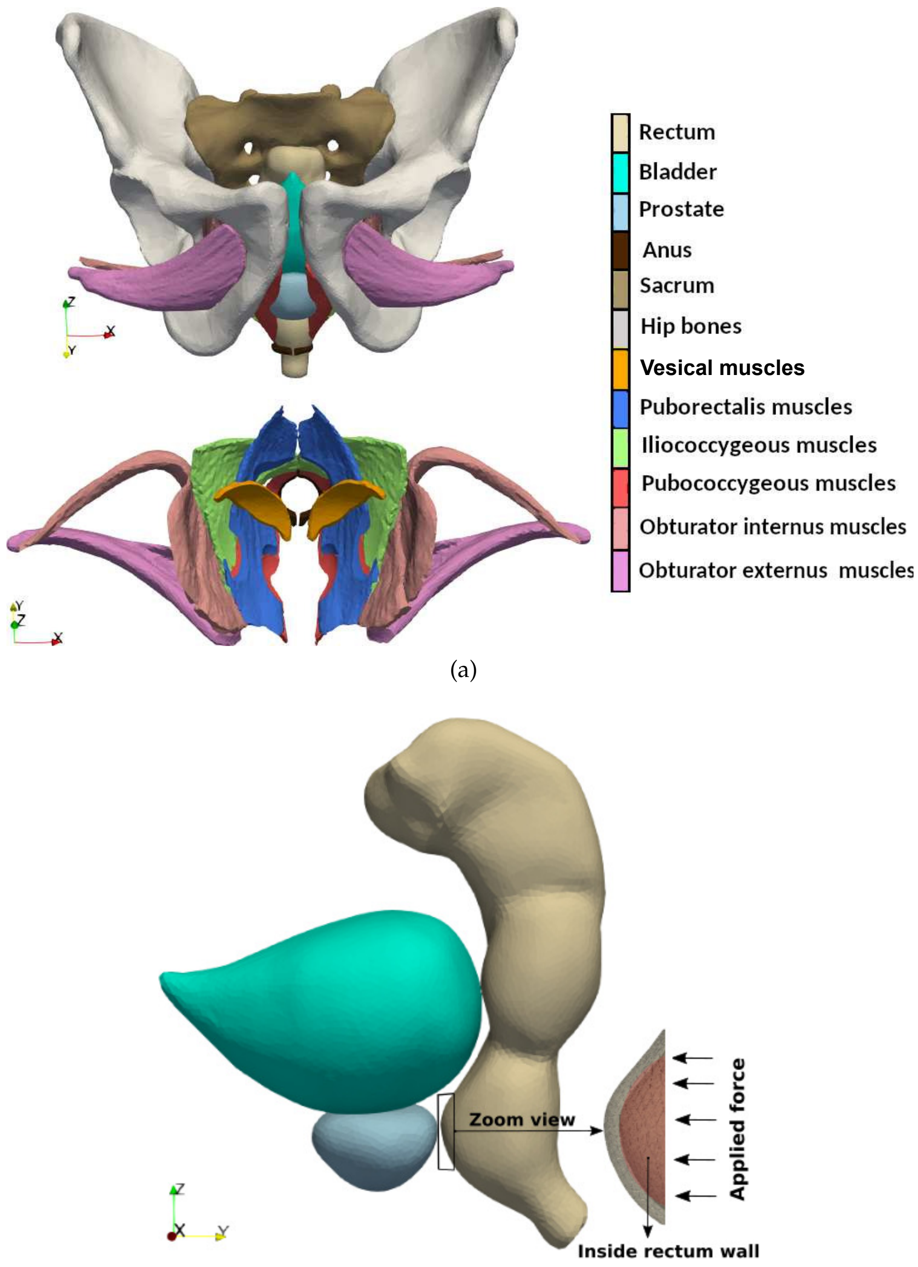

(a)

(b)

Figure 2.1: (a) Transverse view of the geometry model for the pelvic region. For the sake of clarity only the involved muscles are included in the bottom plot. Note that in the frontal body view the X–axis points to the right, the Y–axis points toward the dorsal region and the Z–axis points upwards (into the cranial region). (b) Lateral view of the rectum, bladder and prostate organs with a magnification of the interior region of the rectum where the TRUS probe exerts pressure.

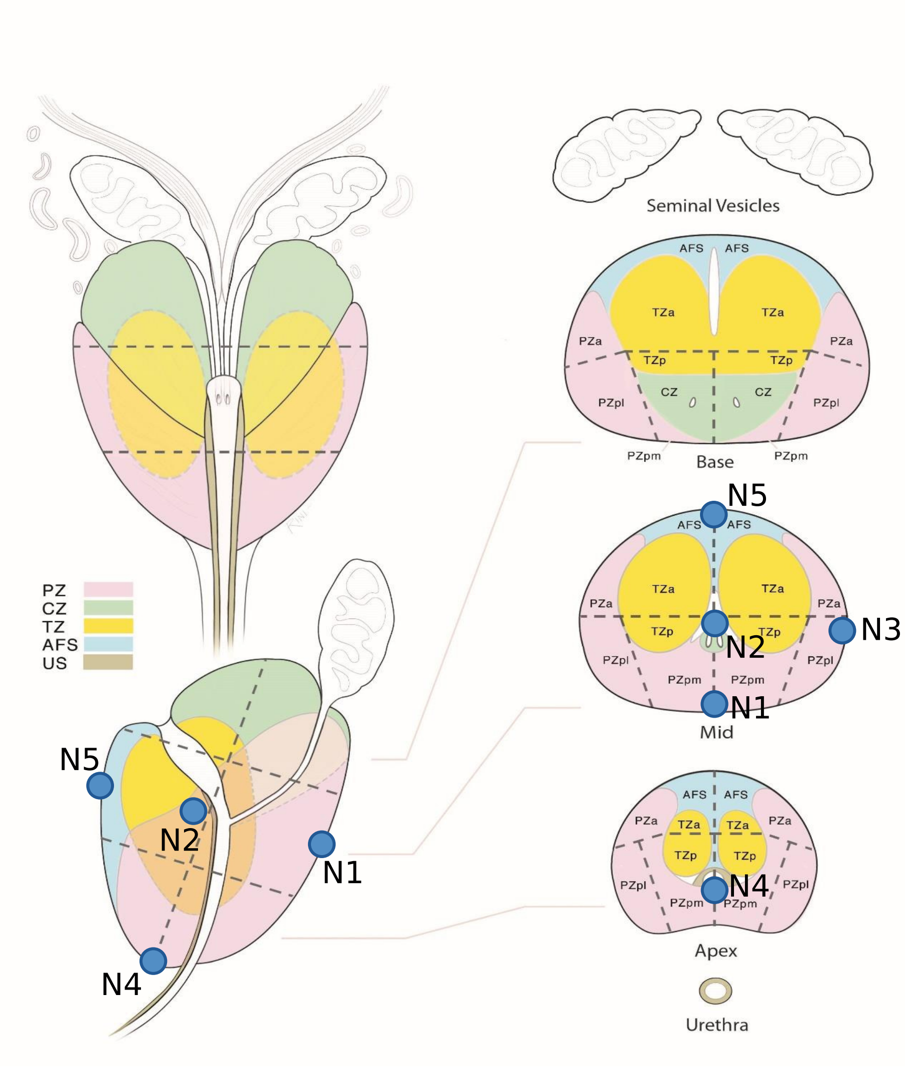

Figure 2.2: Approximate situation of the five selected nodes in the PI-RADS maps [112] as published by the American College of Radiology [3] under a creative commons (CC BY-NC-ND 4.0) license [24]. We have modified the original maps image by superimposing the symbols (circles) and labels denoting the situation of each node.

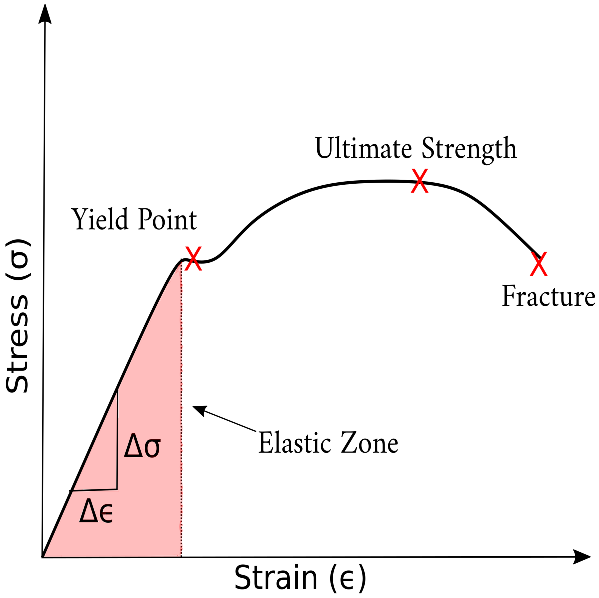

(a)

Figure 2.3: The stress-strain curve and the region of the elastic zone, yield point, ultimate strength, and fracture.

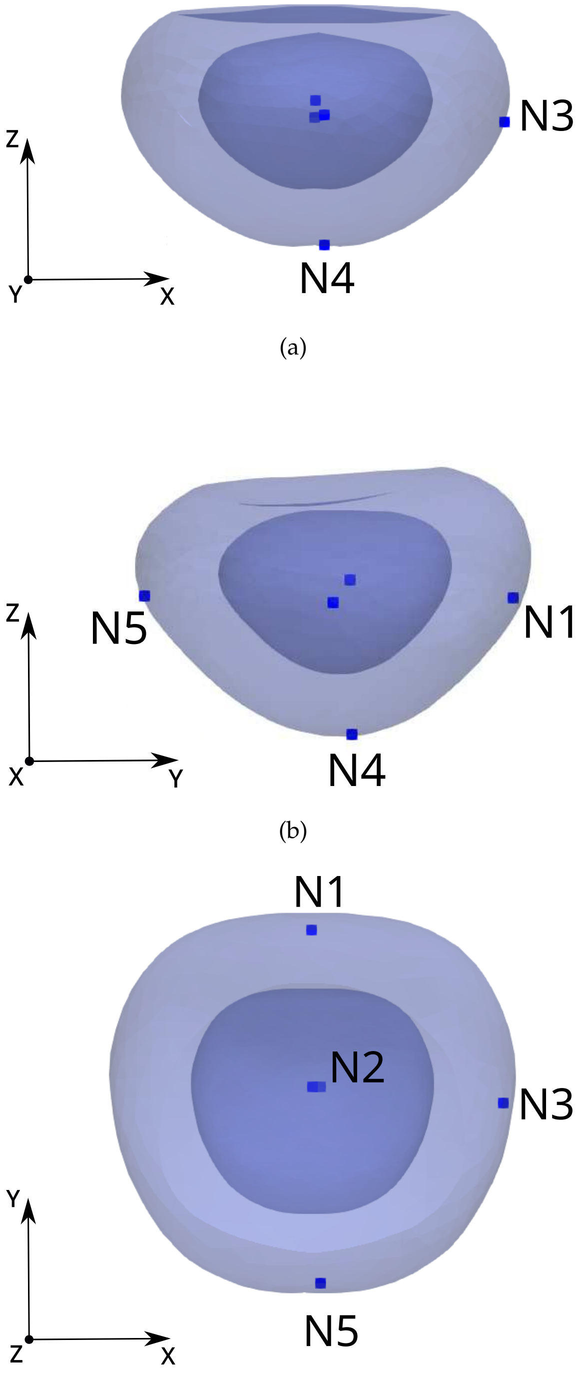

(a)

(b)

(c)

Figure 2.4: Location of the five selected nodes (potentially cancerous lesions) in the prostate. (a) Coronal (posterior) view. (b) Saggital view. (c) Axial view.

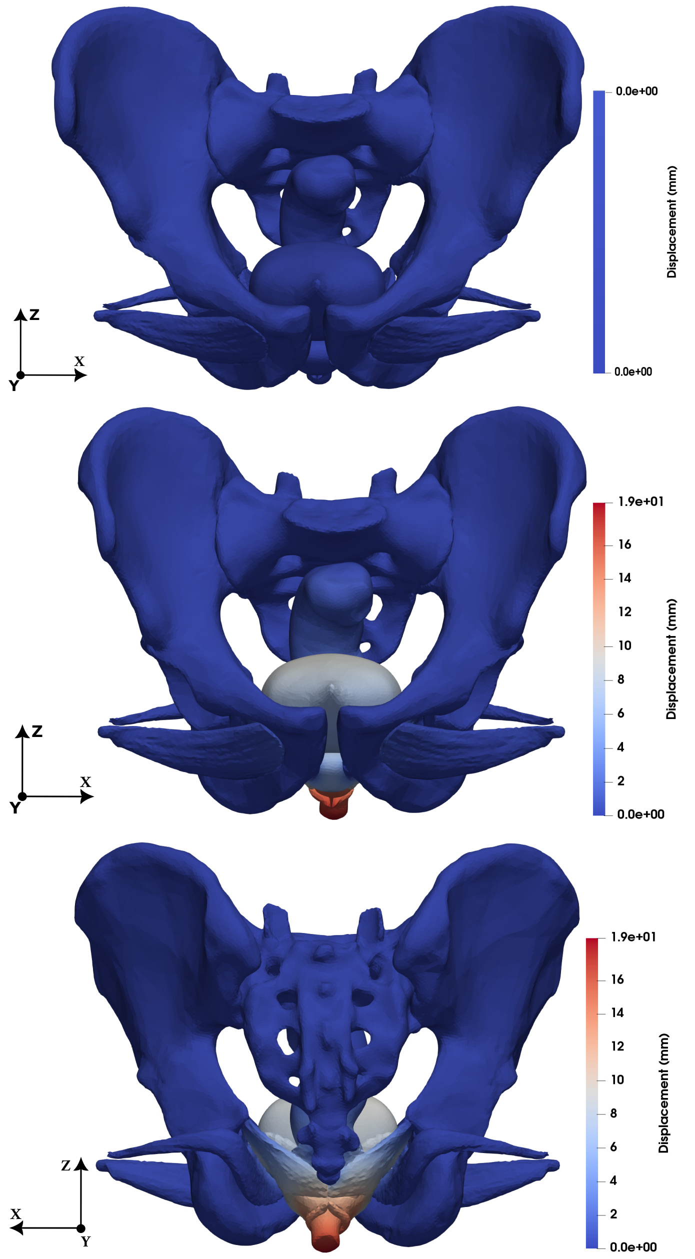

Figure 2.5: The deformation of pelvis organs before (a) and after the influence of TRUS beam pressure at the rectum wall in anterior (b) and posterior views (c) with the displacement values.

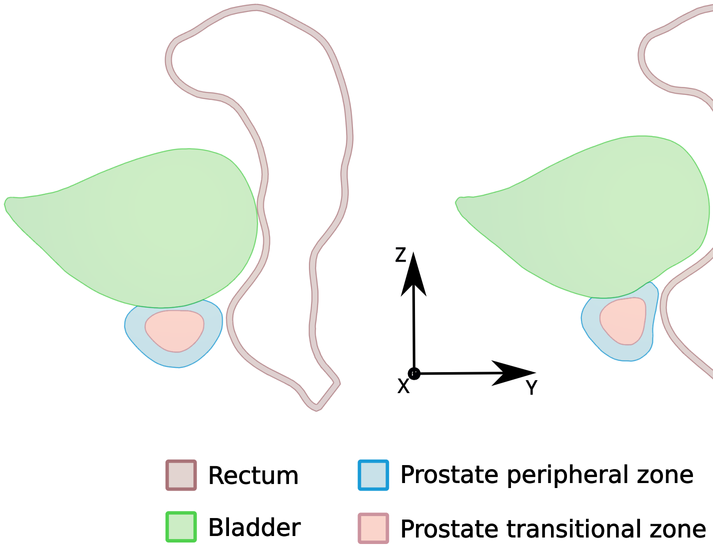

Figure 2.6: Profiles of the rectum, bladder, prostate transitional zone (TZ) and prostate peripheral zone (PZ) in the medial ($X = 0$) plane: original (left) and deformed (right) geometries.

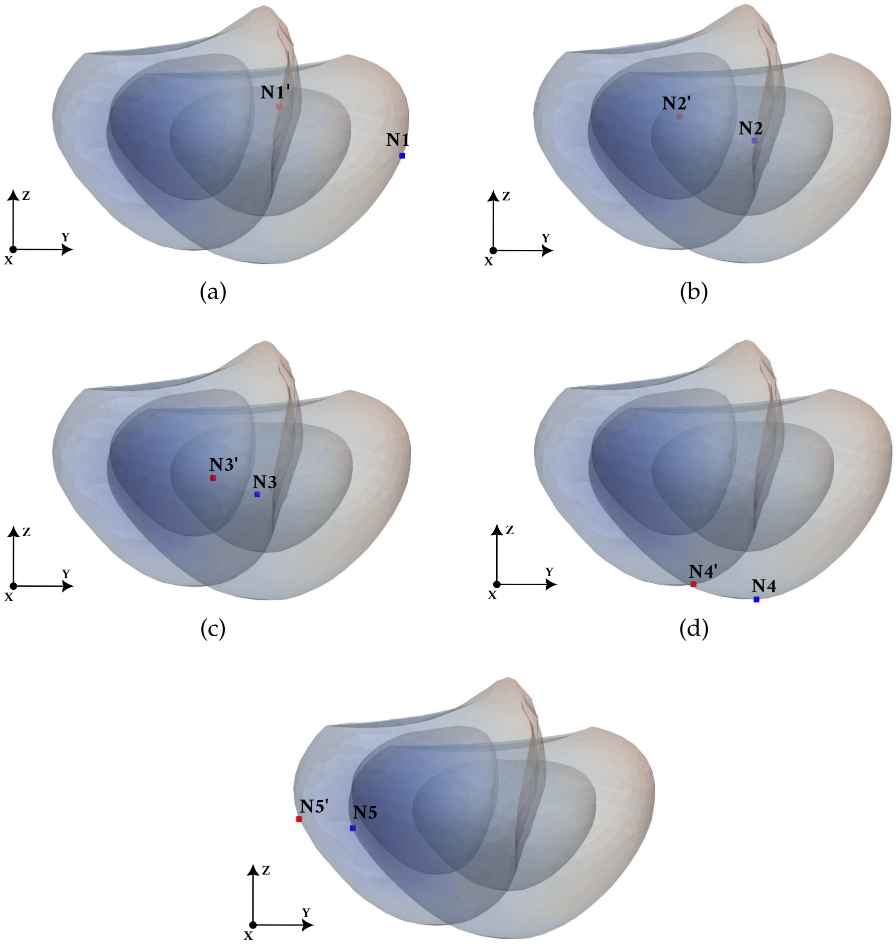

(a) (b)

(c) (d)

(e)

Figure 2.7: Each plot shows the projection of the 3–D original and deformed prostate surfaces into the saggital plane. Blue and red squares respectively denote the initial and final locations of each the five selected nodes: (a) N1, (b) N2, (c) N3, (d) N4 and (e) N5. Note that for the sake of clarity final locations are denoted with a prime added to the node label.

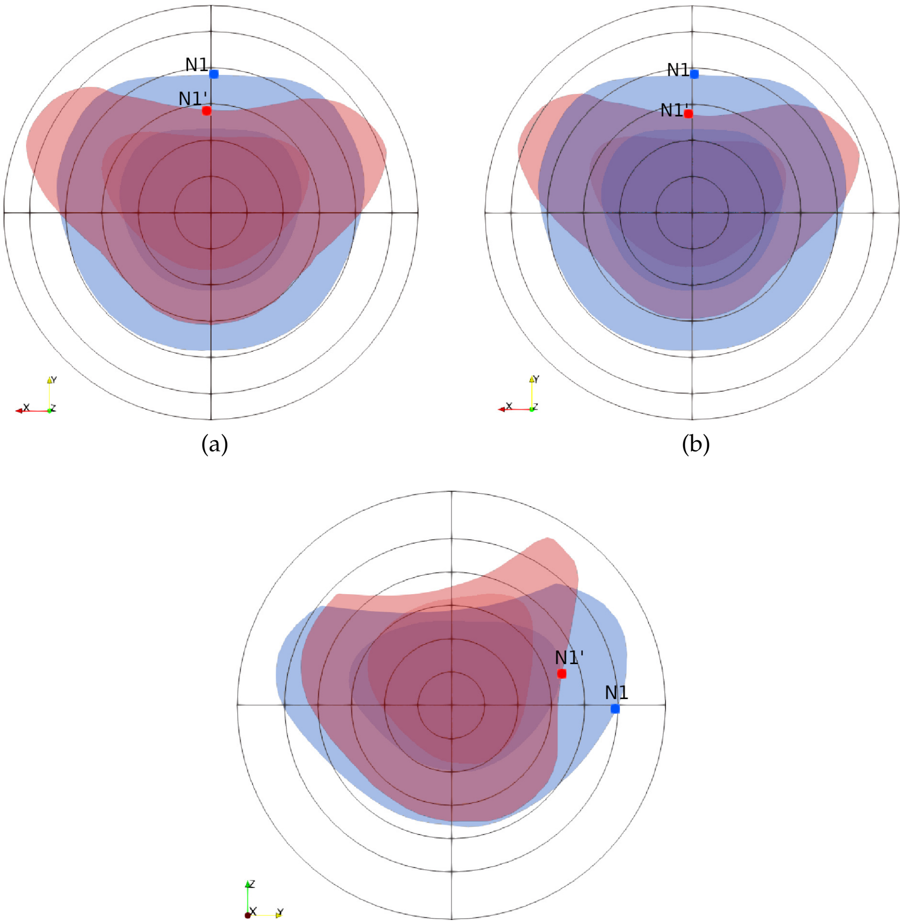

(a)

(b)

(c)

Figure 2.8: Superposition of Original (blue) and deformed prostate in polar coordinates. (a) Axial views with $Z = 0$ for both original and deformed prostate. (b) Axial views taken at the plane where N1 ($N1'$) is located for the original (deformed) prostate. (c) Saggital views taken at the plane where N1 ($N1'$) is located for the original (deformed) prostate.

Chapter 3

Hyperelastic Constitutive Model

Soft biological tissues of male pelvis exhibit complex mechanical behavior, often characterized by stress–strain response. Therefore, modeling pelvis organs is critical to understanding the adjacent relationship of the pelvis structure, which is relevant to the practitioner, urologist or surgeons dealing with prostate biopsy. This chapter aims to provide non–linear mechanical properties of soft tissues (except vesical muscles), which are used for the biomechanical response of pelvis organs induced by TRUS probe pressure. This chapter also compares pelvis organ deformation and prostate lesions displacement with the results obtained in the previous chapter.

3.1 Introduction

The geometry model in Fig. 2.1 is the same realistic model used throughout this chapter. Details on the computational mesh, how it was created, and the conditions used to simulate the clinical practice of a TRUS guided biopsy were the same as in Chapter 2; that is, a force of 30 N to be applied orthogonally to a surface patch of the rectum wall, with an area of 258 mm^2 (see the inset of Fig. 2.1). During the biopsy, the hip and pelvic bones were thought to be immovable. In Chapter 2, all the tissues were assumed to have a linear elastic behavior. However, it is known that the mechanical behavior of soft biological tissues is usually better described by hyperelastic models[49]. Therefore, in this chapter, we assumed an isotropic hyperelastic approach to most of the soft tissues. Numerical simulations were also carried out using the `Code_Aster` open source software.

3.2 Material Models and Methods

In this section, an isotropic hyperelastic approach was used for all the soft tissues, except the vesical muscles that were assumed to have a linear elastic behavior. The reason to omit the vesical muscles from the hyperelastic approach is the lack of experimental data needed to determine the constants involved in hyperelastic models. The constitutive equations were formulated using a quasi–incompressible framework, a predominant formulation in the context of finite element simulations.

Hyperelastic models suppose the existence of a strain energy function (SEF), also known as Helmholtz free energy function. Let the SEF be denoted by W; if the material is modeled as quasi–incompressible then W is commonly decoupled into a volumetric part, W_{vol}, and an isochoric part, W_{ich},

$$W(J,\mathbf{C}) = W_{vol}(J) + W_{ich}(J,\mathbf{C}) \tag{3.1}$$

In Eq. (3.1) $\mathbf{C}$ denotes the right Cauchy–Green tensor defined as $\mathbf{C} = \mathbf{F}^T\mathbf{F}$, being $\mathbf{F}$ the deformation gradient, and J is the determinant of $\mathbf{F}$. The second Piola–Kirchhoff stress tensor, $\mathbf{S}$, is consequently decoupled as

$$\mathbf{S}(J,\mathbf{C}) = \mathbf{S}_{vol}(J) + \mathbf{S}_{ich}(J,\mathbf{C}) \tag{3.2}$$

where the volumetric and isochoric parts are defined as

$$\mathbf{S}_{vol}(J) = 2\left(\frac{\partial W_{vol}}{\partial \mathbf{C}}\right) \tag{3.3}$$

$$\mathbf{S}_{ich}(J,\mathbf{C}) = 2\left(\frac{\partial W_{ich}}{\partial \mathbf{C}}\right) \tag{3.4}$$

Under the isotropy assumption it is known that W depends exclusively on the three invariants of $\mathbf{C}$. That is $W(J,\mathbf{C}) = W(I_1, I_2, I_3)$ with

$$I_1 = tr(\mathbf{C}) = \lambda_1^2 + \lambda_2^2 + \lambda_3^2 \tag{3.5}$$

$$I_2 = \frac{1}{2}\left(tr(\mathbf{C})^2 - tr(\mathbf{C}^2)\right) = \lambda_1^2\lambda_2^2 + \lambda_2^2\lambda_3^2 + \lambda_3^2\lambda_1^2 \tag{3.6}$$

$$I_3 = det(\mathbf{C}) = \lambda_1^2\lambda_2^2\lambda_3^2 = J^2 \tag{3.7}$$

In Eqs. (3.5)–(3.7) λ_1^2, λ_2^2, and λ_3^2 are the three eigenvalues of **C**. It is worth noting that the three invariants are positive and do not depend on the coordinate system. Moreover, the square root of I_3, that is J, represents the change in volume of the material.

A wide variety of hyperelastic models can be found in the literature (see, for example, the review by Chagnon et al. [18]). In the particular case of the hyperelastic polynomial models the isochoric part of the SEF is expressed as

$$W_{ich}(J, \mathbf{C}) = \sum_{i,j=0}^{n} = a_{ij}(I_1 - 3)^i (I_2 - 3)^j \tag{3.8}$$

where a_{ij} are constant coefficients that depend on the material properties and $a_{00} = 0$. When a quasi–incompressible framework is used it is more efficient to implement the constitutive equations in terms of J and the invariants of the modified right Cauchy–Green tensor $\overline{\mathbf{C}} = J^{-2/3}\mathbf{C}$:

$$\bar{I}_1 = I_1 I_3^{-1/3} = I_1 J^{-2/3} \tag{3.9}$$

$$\bar{I}_2 = I_2 I_3^{-2/3} = I_2 J^{-4/3} \tag{3.10}$$

In this study, we used the following formulations for the volumetric and isochoric parts of the SEF

$$W_{vol}(J) = \frac{K}{2}(J-1)^2 \tag{3.11}$$

$$W_{ich}(\bar{I}_1, \bar{I}_2) = a_{10}(\bar{I}_1 - 3) + a_{01}(\bar{I}_2 - 3) + a_{20}(\bar{I}_1 - 3)^2 \tag{3.12}$$

The three–term polynomial formulation for the isochoric part of the SEF in Eq. (3.12) was successfully used by Bhattarai and Staat [8] to model soft tissues in a female pelvic floor. Among the multiple volumetric functions that have been suggested in the literature (see [32] for a discussion about the fulfillment of relevant physical conditions of some widely used volumetric functions) we opted by the quadratic function defined in Eq. (3.11).

Table 3.1: Characteristics of the experimental samples.

Reference	**Tissue**	**Sample geometry (mm)**
Rubod et al. (2012) [93]	Rectum	15 × 4 × 1.5
Janda et al. (2006) [54]	Pelvic floor muscles	15 × 3 × 3
Ma et al. (2012) [64]	Prostate (transitional zone (TZ))	$9.5 \pm 2.2 \times 2.0 \pm 0.6 \times 1.7 \pm 0.5$
Johnson et al. (2020) [55]	Prostate (peripheral zone (PZ))	Intact human specimen with an average surface area of 2025 (± 671) mm^2 and height of 33 (± 1.9)

In order to obtain the particular form of **S** for the SEF formulation (3.11)–(3.12) we use the chain rule:

$$\mathbf{S}_{vol} = 2\left(\frac{\partial W_{vol}}{\partial J}\frac{\partial J}{\partial \mathbf{C}}\right) \tag{3.13}$$

$$\mathbf{S}_{ich} = 2\left(\frac{\partial W_{ich}}{\partial \bar{I}_1}\frac{\partial \bar{I}_1}{\partial \mathbf{C}} + \frac{\partial W_{ich}}{\partial \bar{I}_2}\frac{\partial \bar{I}_2}{\partial \mathbf{C}}\right) \tag{3.14}$$

along with the following derivatives:

$$\frac{\partial J}{\partial C_{ij}} = \frac{1}{2} J C_{ij}^{-1} \tag{3.15}$$

$$\frac{\partial \bar{I}_1}{\partial C_{ij}} = I_3^{-\frac{1}{3}}\left(\delta_{ij} - \frac{1}{3} I_1 C_{ij}^{-1}\right) \tag{3.16}$$

$$\frac{\partial \bar{I}_1}{\partial C_{ij}} = I_3^{-\frac{2}{3}}\left(I_1\delta_{ij} - C_{ij} - \frac{2}{3} I_2 C_{ij}^{-1}\right) \tag{3.17}$$

Therefore the final expression for **S** can be written as

$$\begin{aligned} S_{ij} =& K(J-1)JC_{ij}^{-1} + 2\left(a_{10} + 2a_{20}(\bar{I}_1 - 3)\right) I_3^{-\frac{1}{3}}\left(\delta_{ij} - \frac{1}{3} I_1 C_{ij}^{-1}\right) + \\ & 2a_{01} I_3^{-\frac{2}{3}}\left(I_1\delta_{ij} - C_{ij} - \frac{2}{3} I_2 C_{ij}^{-1}\right) \end{aligned} \tag{3.18}$$

3.2.1 Material coefficients

The quality and accuracy of mechanical simulations rely upon an appropriate characterization of involved tissues. The classical approach for the mechanical characterization of tissues consists on fitting stress–strain curve predicted by FE simulations to measurements available in the literature. It should be noticed that experimental data on the mechanical properties of tissues in the pelvic region are limited. Therefore, we had to make some assumptions and we had to use data obtained from different experimental testing protocols. In particular, experimental data based on the tensile testing protocol were available for the following soft tissues: rectum [20], bladder [67], pelvic floor muscles [54] and prostate transitional zone (TZ) [64]. Instead the available experimental measurements for the prostate peripheral zone (PZ) were based on the probing testing method [55]. Furthermore, the lack of more detailed data for the pelvic muscles lead us to assume the same mechanical behavior for all these muscles and the absence of data forced us to consider a linear model for the vesical muscles.

In the case of uniaxial tensile tests a thin rectangular tissue sample is fixed on one lateral edge and is pulled on the opposite one. During this process, the elongation of the sample is recorded against the applied force. Stress and strain are respectively calculated as $\frac{F}{A_0}$ and $\epsilon = \frac{\Delta L}{L_0} = \frac{L-L_0}{L_0}$, where F is the tensile force, A_0 is the initial cross–sectional area at which force is applied, ΔL is the change in the sample length, L_0 is the initial sample length and L is the final sample length. In the case of probing (indentation) testing a rigid probe is pushed into the surface of a tissue. Force and displacement are sampled and recorded throughout the experiment and subsequently transformed into stress and strain. In this case the stress is calculated as $\frac{F}{A_p}$ where A_p is the surface area of the probe.

`Code_Aster` FE software to perform numerical simulations that recreated each one of the aforementioned experimental testings [20, 67, 54, 64, 55]. For this purpose first 3–D computational meshes are generated, reproducing the tissue samples used in each experimental situation (see Tab. 3.1 for details). Then several numerical computations are run with different values of the material coefficients, a_{10}, a_{01} and a_{20}, and trial and error approach were used to find the coefficients that best fitted the stress–strain experimental data.

In the simulations we prescribed boundary conditions that emulated the experimental procedure. Moreover, in the particular case of the experiments of Johnson et al.[55], to simulate the probing test with a flat circular probe (0.0049 m diameter), we defined a roughly circular surface of 0.0182 m^2 located on the top region ($-Y$ direction) of the peripheral prostate at which force was applied. The total surface area and height of our 3-D prostate is 28064 mm^2 and 31.7 mm, respectively, which is similar to the geometry given in the Table 3.2.

3.2.2 Simulation Results

The non-linear behaviors of most of the soft tissues are illustrated in stress–strain curves in Figs. 3.1–3.3 and the material coefficients $(a_{10}, a_{01}$ and $a_{20})$ used to define the biomechanical response of a specimen are displayed in Table 3.2. We adopted the biomechanical properties of the bladder from the study of Bhattarai et al. [8] due to lack of mechanical data on the human bladder. The pelvic floor muscle's response of the uniaxial stress-strain responses (raw data fits) of the three specimens derived from cadaveric muscles is shown in Figure 3.3 (Janda et al. [54]). However, we used the average experimental curve from the specimens for the numerical data, which is similar to the findings of another study [78].

We observed almost the same stress-stress relationship of prostate PZ and prostate TZ geometries with the constant values of a_{10}, a_{01} and a_{20} in the low strain region $(< 5\%)$. However, the tissue geometries of the rectum and pelvic floor muscles, which have greater a_{10} values are stiffer in this region. Examining the influence of a_{20}, we noticed that larger a_{20} leads to more non-linear stress-strain response as tissues and organ geometries are stretched under uniaxial tension or probing. Overall, the tissue geometry of the rectum showed more rigidity than was the geometry of pelvic floor muscles, which in turn was more rigid than prostates geometries.

Table 3.2: Values of the material coefficients a_{10}, a_{01} and a_{20} in the constitutive model (3.11) that produce the best fitting to experimental data for each tissue.

	Material coefficients		
Tissue geometry	a_{10} (MPa)	a_{01} (MPa)	a_{20} (MPa)
Rectum	0.275	0.0	3.5
Bladder	0.0835	0.0	0.092
Pelvic floor muscles	0.0085	0.0	0.35
Prostate transitional zone (TZ))	0.005	0.0	0.28
Prostate peripheral zone (PZ)	0.0005	0.0	0.01

For the simulations of pelvis model (Fig. 2.1), we implemented the parametric values of soft tissues (given in Tab. 3.2) into the Signorini hyperelastic model. Only pelvic bones

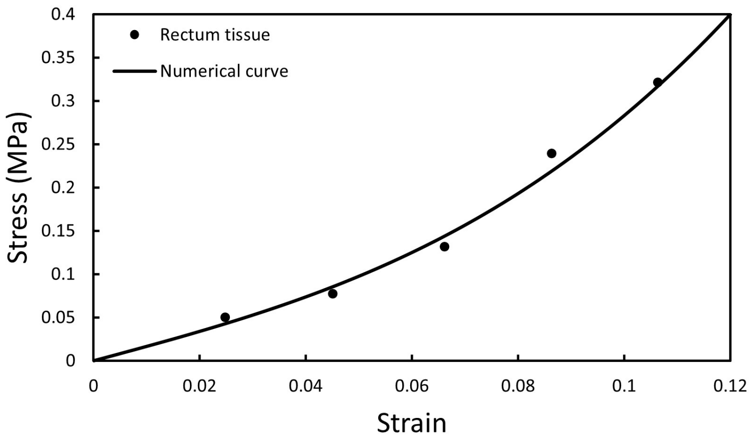

Figure 3.1: Fitting of rectum tissue data with three term Signorini hyperelastic constitutive model. Curve with line show numerical results

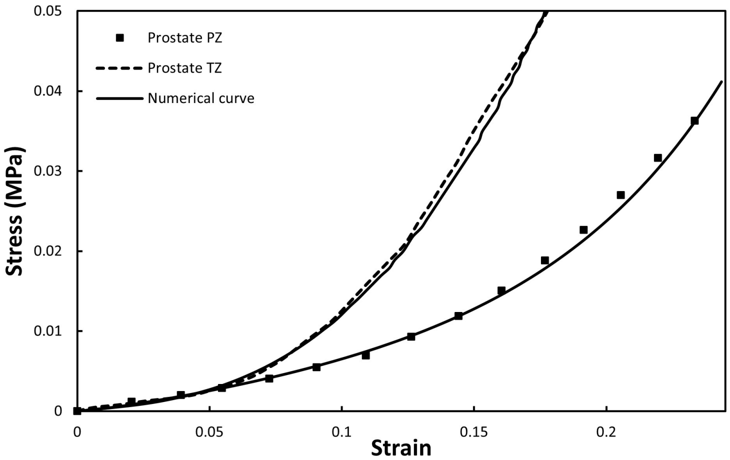

Figure 3.2: Fitting of peripheral and transitional prostates with three term Signorini hyperelastic constitutive model. Curves with line show numerical results

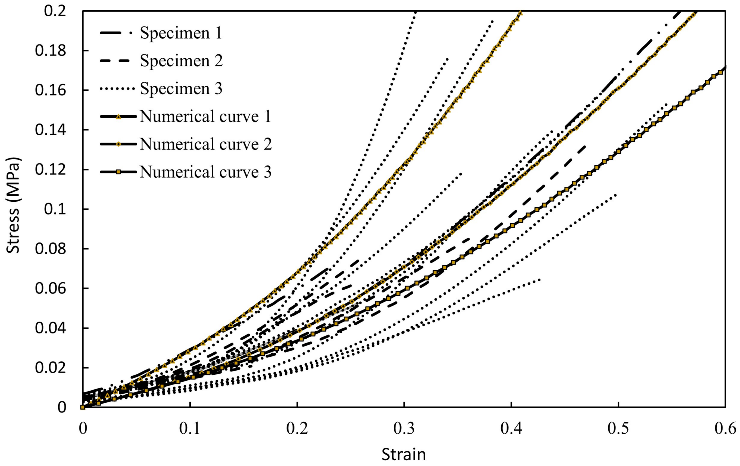

Figure 3.3: Uniaxial stress–strain responses of the pelvic floor muscles taken from Janda et al. [54] and numerical curves with line shows fitting with three term Signorini hyperelastic constitutive model

and vesical muscles are assumed to be linearly elastic and given the same values described in Table 2.1.

Figures 3.4–3.6 depicted the outcome of a biomechanical model when a TRUS probe force of 30 N was applied at the rectum wall. The figure's legend color from blue to red describes the values of displacements, low to high. The rectum shows the highest displacement of 14 mm towards the -Y direction because of the TRUS probe force's first contact at the rectum side's area. As a result, in an antecedent direction, significant non-uniform deformation was observed of the prostate peripheral and transitional zone of approximately 11.5 mm and 10 mm. At the same time, the bladder deformed 7 mm in the +Z axis direction, where the prostate and bladder intersect. The pelvic floor muscles, assumed above the same mechanical behavior of all tissues, showed displacement values ranging from 0 to 12 mm, as shown in Fig. 3.5. Where the highest displacement (12 mm) was observed on pubococcygeous muscles at the area; where it surrounds the rectum, closer to the area where force is applied on the rectum wall. According to the assumptions and rigidity of pelvic bones [91], there were exactly zero displacements on the hip and sacrum bones.

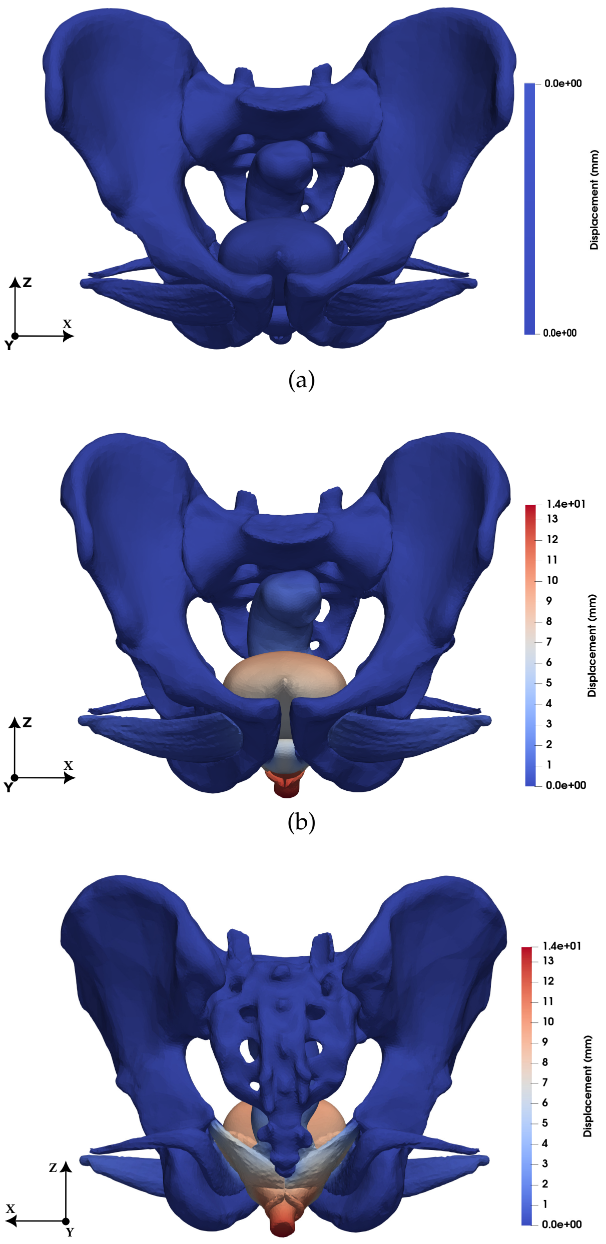

(a)

(b)

(c)

Figure 3.4: The deformation of pelvis organs before (a) and after the influence of TRUS beam pressure at the rectum wall in anterior (b) and posterior views (c) with the displacement values.

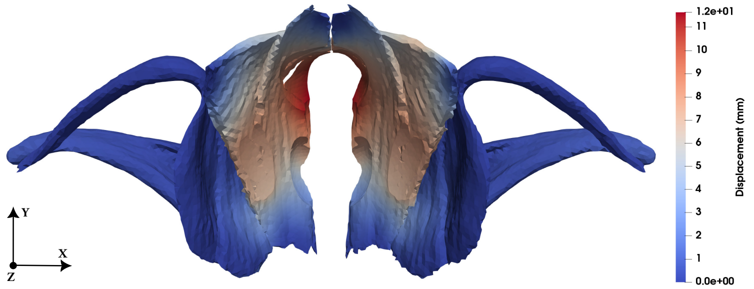

Figure 3.5: Pelvic muscles deformations after the influence of TRUS beam pressure at the rectum wall.

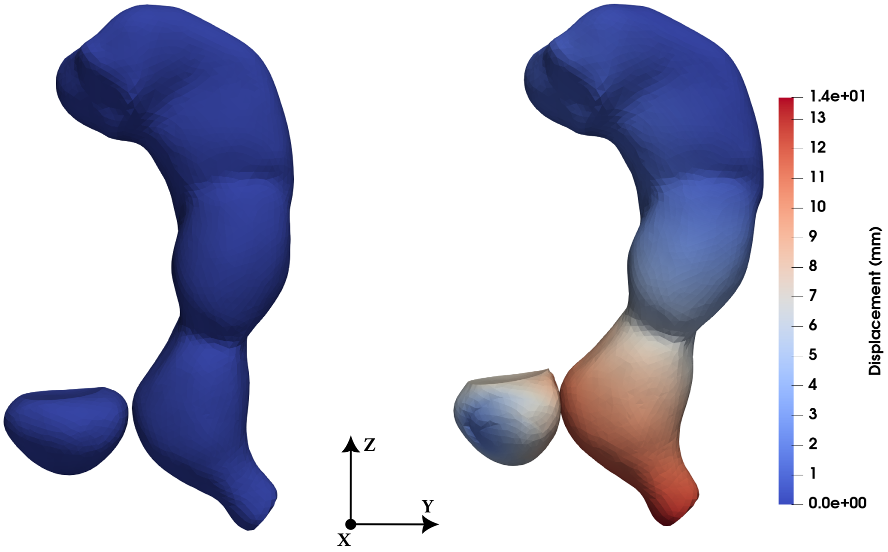

Figure 3.6: Profile of rectum, bladder and prostates in the sagittal plane: original (left) and deformed (right) geometries.

3.3 Comparisons and Discussions

This section compares pelvis organs deformation between linear elastic (Chap. 2) and hyperelastic biomechanical models, focusing on the prostate's five mesh node displacements. In non-linear case, the rectum showed less displacement than in the linear elastic simulation because of the stiff mechanical properties of the prostate (see Fig. 3.6). Human tissues are not routinely accessible for research due to the slow rate of human studies and the fact that interventional trials are few and far between [41]. Therefore, we could not find the mechanical properties of tissues related to the one given in Chapter 2, as the mechanical properties are different and non-identical in-between each organ. For example, in the case of Janda et al. [54] experiments, the same specimen tissue has non-identical properties, as shown in Fig. 3.3.

All the pelvic tissues and organs behaved similarly to the rectum in terms of displacement values, i.e., less displacement values than in Chap. 2. Compared to the displacements in Chap. 2, the bladder, prostate PZ and TZ displacement values varied by approximately 2 mm, 3.5 and 2 mm, respectively. Similarly, the pubococcygeus muscles showed less displacement values in hyperelastic case and a difference of 3 mm displacement in values are observed.

Fig. 3.7 shows the prostate motion and deformation due to the TRUS probe force impact; before (undeformed) and after (deformed). The left and right column figures compare the prostate deformation of two simulation results, linear elastic and hyperelastic. The node (N1, N2, N3, N4, and N5) represents small lesions' at each prostate's initial location while the nodes with prime show the final position within the prostate. For example, node N1 is in the initial state; before the biopsy, while node N1′ is the final location when the biopsy force of 30 N is applied. We can see that the prostate deformation that comes from the linear elastic properties is more in cranially upward (along with $-Y$) direction compared to the hyperelastic properties of the prostate.

Table 3.3: Coordinate displacements and their magnitudes of prostate lesions w.r.t. nodes after applying TRUS pressure at the rectum wall. The hyperelastic and linear–elastic displacements are obtained when non–linear and linear material properties are applied to the organs.

		Hyperelastic displacements (mm)				Linear-elastic displacements (mm)			
Node	Location in prostate	*DX*	*DY*	*DZ*	Magnitude	*DX*	*DY*	*DZ*	Magnitude
N1	PZ midsaggital, intermediate level	0.46	-10.60	3.32	11.12	0.94	-12.91	5.16	13.93
N2	TZ midsaggital, intermediate level	0.44	-7.11	3.50	7.94	-0.66	-7.84	2.52	8.26
N3	PZ lateral, intermediate level	1.86	-3.93	3.11	5.35	3.37	-4.56	1.70	5.20
N4	PZ midsaggital, apex level	0.51	-6.47	2.36	6.90	0.68	-6.56	1.56	6.78
N5	PZ midsaggital anterior, intermediate level	0.51	-5.21	2.38	5.76	0.34	-5.53	0.94	5.61

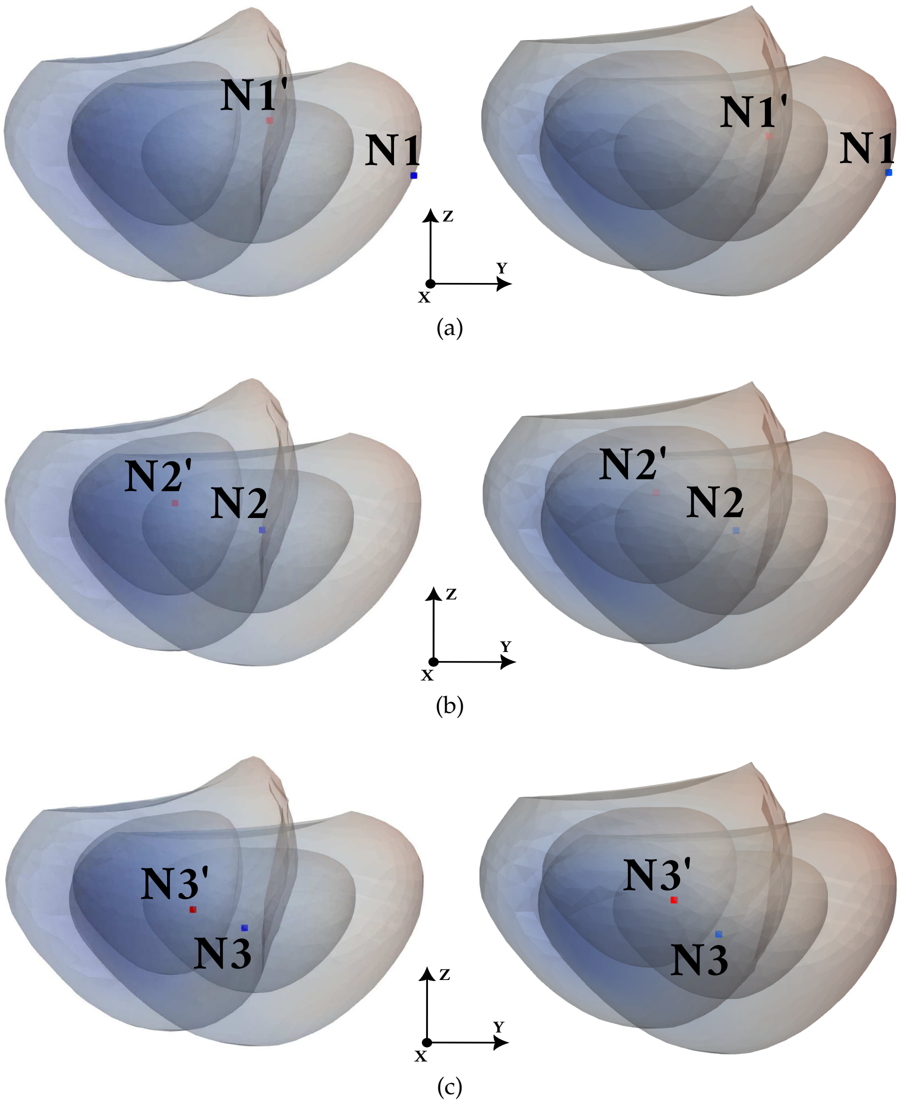

(a)

(b)

(c)

Table 3.3 describes the information of node's displacements and their magnitudes in-between two biomechanical simulations (linear elastic and hyperelastic). In both simulations, node N1, located at the midsaggital zone of the peripheral prostate, lies directly in front of the rectum wall where probe pressure is applied, causing the highest displacements. In contrast, node N3 experienced low displacements due to the constraints of puborectalis and pubococcygeus muscles. The distance traveled by the nodes in terms of

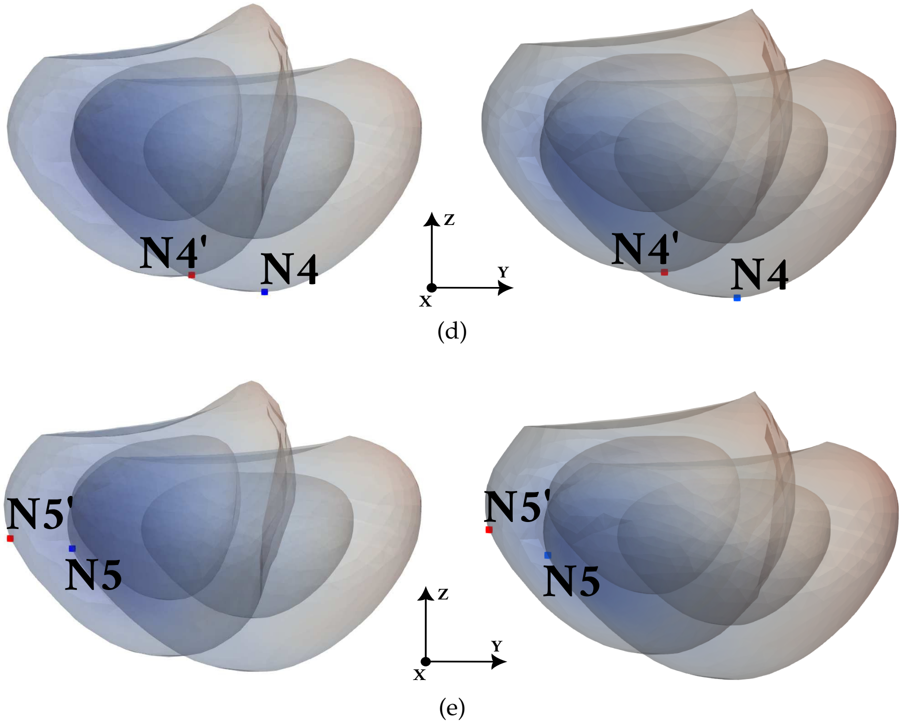

Figure 3.7: Each plot shows the projection of the 3–D original and deformed prostate surfaces into the saggital plane. Blue and red squares respectively denote the initial and final locations of each the five selected nodes: (a) N1, (b) N2, (c) N3, (d) N4 and (e) N5. The left and right figures compare the projections obtained in previous and current chapters.

displacement magnitude ranges from 5.35 to 11.12 mm in the hyperelastic case and from 5.20 to 13.93 mm in the linear elastic case, respectively.

Figs. 3.8 represents the superimposed slices of the original (blue color) and deformed prostate (red color) in polar coordinate; an MRI-TRUS registration method would generate when tracking the N1 node. We already discussed the idea behind the superimposition of slices in Chap. 2. The slices acquired using the prostate's linear–elastic properties are presented on the left side of Figs. 3.8, whereas the slices created using the hyperelastic approach are shown on the right side. Fig. 3.8 (a) shows the superposition of slices in the axial plane, while maintaining the same plane of the deformed and undeformed prostate slices at Z = 0, where the lesions were observed in the original MRI images. Similarly, in Fig. 3.8 (b), the overlaying of slices is demonstrated by keeping the deformed and undeformed prostates on their original axes.

As can be seen in Figs. 3.8 (a and b), the undeformed slices (blue color) in both cases (linear elastic and hyperelastic) have the same sizes. However, the deformed slices (red color) show different behavior. For example, if we look at the deformed slices in the hyperelastic case, we see that the slices are less outside the contour of the original slice because the prostate is deformed less along the pelvis muscles. When both slices are taken in the saggital plane at the original (deformed) prostate (right Fig. 3.8 (c)), the node N1 has the displacement values along the X, Y and Z axis are 0.94 mm, -12.91 mm, 5.16 mm, respectively. The displacement of node N1 along the X axis is almost half as compared to the linear elastic case. Similarly, the displacement differences along the Y and Z axis are -2.31 mm and 1.84 mm, respectively. The difference is due to the stiff mechanical properties of the prostate, bladder (along the Z-axis) and pelvic muscles (along the X-axis). This information gives the practitioner an extra layer of knowledge about the contour of the targeted node.

3.4 Conclusions

In this chapter, we obtained the biomechanical FE simulation of pelvis model with hyperelastic properties of soft tissues except for vesical muscles. We used the Signorini hyperelastic model for the mechanical characterization of soft tissues to fit the stress–strain curves available in the literature. Moreover, we compared pelvis organ deformations and prostate lesions displacement with the values obtained in the previous chapter.

Our finding indicates that the tissue geometry of the rectum showed more rigidity than was the geometry of pelvic floor muscles, which in turn was more rigid than prostates geometries. Also, simulating the pelvis model induced by TRUS motion provides deformation of pelvis organ and lesions displacement of the prostate are less compared to the previous study. In linear elastic and hyperelastic simulations, the rectum showed the largest deformations of 19 mm and 14 mm among the other pelvic organs, respectively. Similarly, the maximum and minimum displacement values are observed for nodes N1 and N3. The differences in the displacement values (in between linear elastic and hyperelastic simulations) of these nodes are 4.91 and 1.43 mm, at the midsaggital and lateral region of the peripheral zone of the prostate.

Overall, this updated methodology allowed us the prediction of prostate lesions during a TRUS-guided biopsy when the mechanical behavior of tissue organs is implemented.

However, the numerical results are not close to the values obtained using linear-elastic material models. It has been proved in different studies that the same human tissue possesses different mechanical properties. A fully nonlinear model is necessary when more accurate estimates of pelvis deformation and prostate neoplasms displacement are required, for example, to assess the potential of tensile strength or elastic properties.

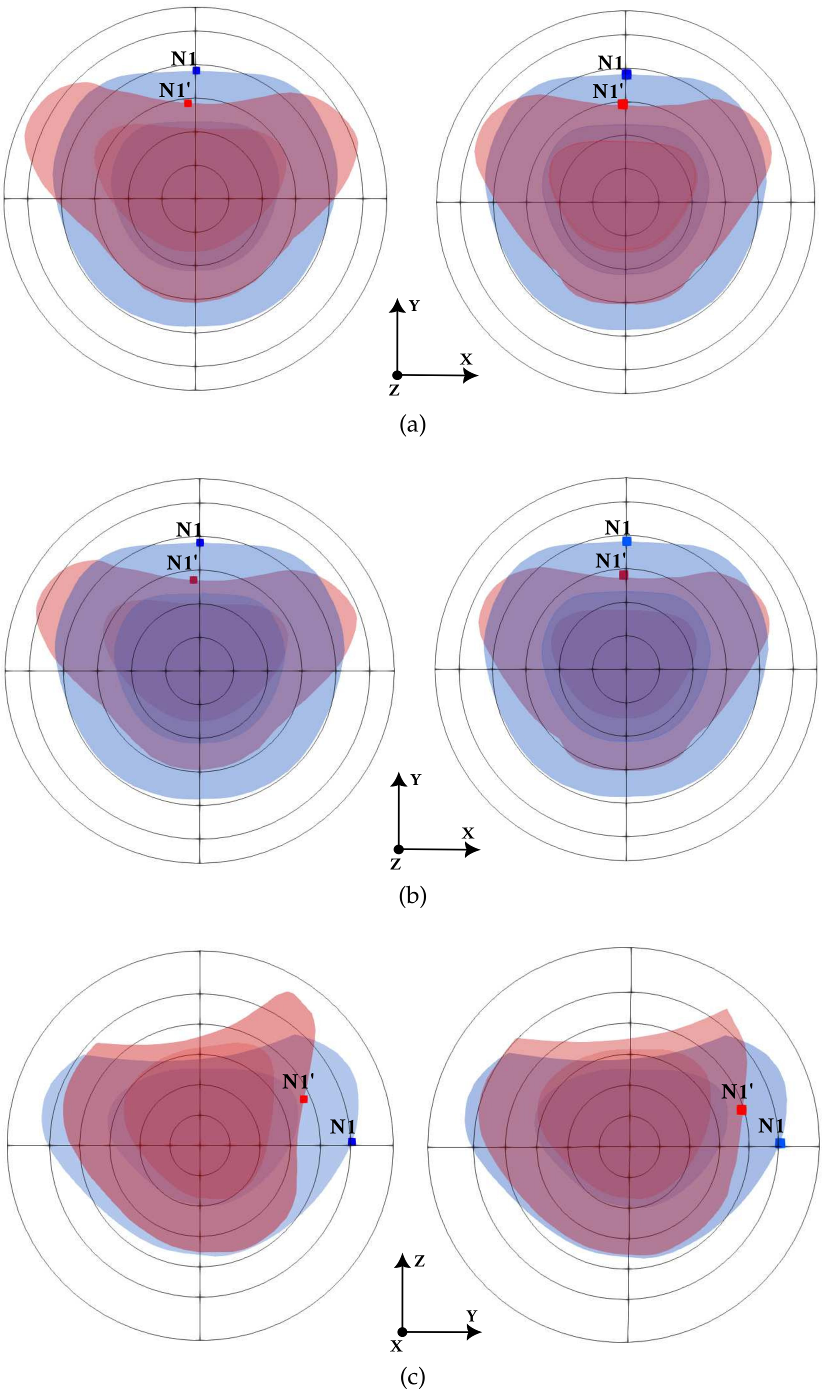

(a)

(b)

(c)

Figure 3.8: Superposition of Original (blue) and deformed prostate in polar coordinates. (a) Axial views with $Z = 0$ for both original and deformed prostate. (b) Axial views taken at the plane where N1 (N1$'$) is located for the original (deformed) prostate. (c) Saggital views taken at the plane where N1 (N1$'$) is located for the original (deformed) prostate. The left and right figures compare the slices obtained in previous and current chapters.

Chapter 4

Anisotropic-Viscoelastic Model

This chapter will present a 3-D computational model of the human prostate, focusing on the prostate geometry, fiber orientation and strain rate at 25%. It will also include the new constitutive model for the anisotropic viscoelastic behavior of prostate geometry. The new model will be the independence of the anisotropic and viscoelastic parts which are based on polynomial functions of certain invariants quantities. This chapter will also discuss implementing the anisotropic-viscoelastic model into the open-source software `Code_Aster` *and* `MFront` *code.*

4.1 Introduction

The mechanical behavior of soft biological tissues is usually characterized by time-dependent, non-linearity, anisotropy and viscoelasticity. These behaviors are demonstrated in mechanical testing when the material exhibits stress relaxation and rate-dependent hysteresis under cyclic loading. Since material characteristics depend heavily on the direction of loading, it is considered an anisotropic nature [34]. In medical image computing, such as biomechanically-driven image registration [88] and interactive surgical simulation, efficient and precise methods for simulating soft biological tissues are becoming an increasingly important tool [110].

The fundamental causes of viscoelasticity of soft tissues depend on the tissue of interest and are categorized into three areas; fibrous network (contains fluid flow), transient network (connections between protein, sugar molecule and collagen network) and individual components in the extracellular matrix (like collagen and elastin fibers) [9]. The variety of research on biological tissues was carried out in the past, such as cartilage [73], cartilaginous tissues [109], ligament [**Pe\IeC {\~n}a2007**, 87], posterior cruciate ligament

[61, 62], ligaments and tendons [118], porcine liver tissue [23], arterial walls [47], cat lungs [76], aortic valve [5], brain tissue [69], abdominal muscles [113] and among others.

However, limited research has been done on the mechanical testing of prostate tissues. Krouskop et al. [58] was the first reported mechanical testing for the breast and prostate tissues. The mechanical stress relaxation data obtained from human prostate tissue samples were characterized by Hoyt et al. [50] using the Kelvin–Voigt fractional derivative (KVFD) viscoelastic model. The findings of that mechanical test revealed that the viscosity parameter for cancerous prostate tissue is approximately 2.4 times greater than the one obtained in normal prostate tissue. Johnson et al. [55] characterized the mechanical properties of human and porcine prostate using probing and compression testings. No statistical differences were seen between the elastic modulus of human and porcine prostate, but the elastic modulus depends on strain rates.

The constitutive model of the human prostate plays a key role in the simulation of its mechanical behavior. Therefore, the main aim of this work is to develop a constitutive model and its implementation that allows for simulating the mechanical behavior of the human prostate under probing technique. To simulate the behavior of human prostate [55], it is necessary to consider the fiber direction described in Sinha et al.[103], which in our case, in the Z-direction of prostate geometry (see Fig. 4.2).

The kinematics of the constitutive models start dealing with the relation of the deformation gradient. The reference configuration is the domain of the body in the initial state represented by Ω_0. The domain in the current configuration is denoted by Ω. Let's assume that a material particle $\mathbf{X}$ is in the original state Ω_0 moves to the final state $\mathbf{x}$ in the current configuration domain Ω at time t (see Fig. 4.1). Then the deformation gradient is represented as $\mathbf{F} = \frac{\partial \mathbf{x}}{\partial \mathbf{X}}$ and the modified deformation gradient is $\overline{\boldsymbol{F}} = J^{-\frac{1}{3}}\mathbf{F}$, where J is the determinant of $\mathbf{F}$.

In recent years, new constitutive models have been proposed [113, 63] to reproduce the loading test data in the corresponding FE numerical simulations. Tuset et al. [113] presents a new formulation of the transversely isotropic hyperelastic model (TIHM) to study the abdominal wall tissue. In TIHM model, the SEF is composed of isotropic $\overline{\psi}_{iso}$ and fiber $\overline{\psi}_{fib}$ contribution terms which further characterized by polynomial functions of the invariants of $\overline{\mathbf{C}}$ and $\mathbf{a}_0 \otimes \mathbf{a}_0$. The new model involved two modified invariants ($\overline{I}_1$, $\overline{I}_4$)

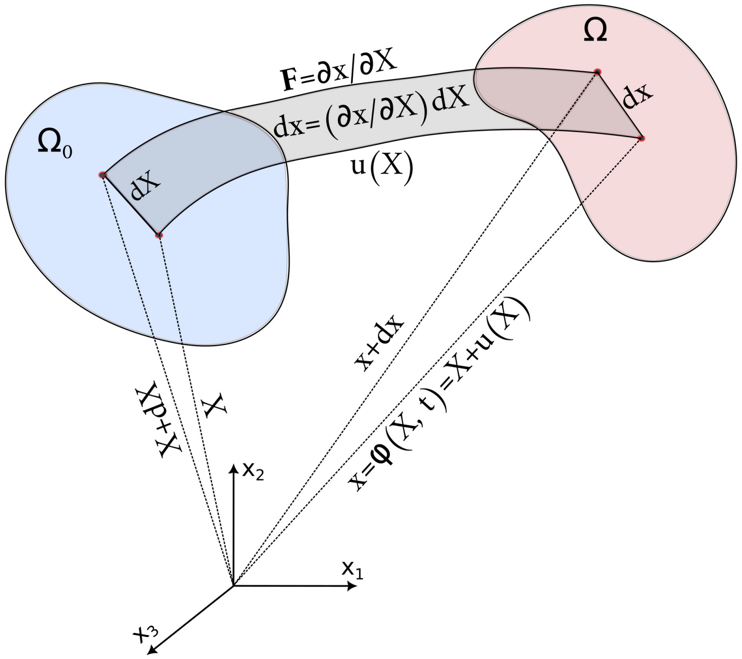

Figure 4.1: The motion of a continuum body.

and four constants (C_1, C_2, C_3 and C_4) defined as:

$$\overline{\psi}\left(\overline{I}_1,\ \overline{I}_4\right) = \underbrace{C_1\left(\overline{I}_1 - 3\right) + C_2\left(\overline{I}_1 - 3\right)^2}_{\text{isotropic–part}} + \underbrace{C_3(\overline{I}_4 - 1)^2 + C_4(\overline{I}_4 - 1)^4}_{\text{fiber–part}} \tag{4.1}$$

and the volumetric contribution is $U(J) = \frac{1}{2}K\left(J^2 - 1 - 2\ln J\right)$. The derivatives of the invariants are described for the second Piola–Kirchhoff stress tensor, **S**, in the article [113] as

$$\frac{\partial \overline{I}_1}{\partial \overline{C}} = \mathbf{I} \tag{4.2}$$

$$\frac{\partial \overline{I}_4}{\partial \overline{C}} = \mathbf{a}_0 \otimes \mathbf{a}_0 \tag{4.3}$$

Then the stress tensor (**S**) is given in the study of Tuset et al. [113] by:

$$\overline{\mathbf{S}} = \overline{\gamma}_1\mathbf{I} + \overline{\gamma}_2\mathbf{a}_0 \otimes \mathbf{a}_0 \tag{4.4}$$

where $\overline{\gamma}_1$ and $\overline{\gamma}_2$ are the derivatives of Eq. 4.1 like

$$\overline{\gamma}_1(\overline{I}_1) = 2\frac{\partial \overline{\psi}_{iso}}{\partial \overline{I}_1} \tag{4.5}$$

$$\overline{\gamma}_2(\overline{I}_2) = 2\frac{\partial \overline{\psi}_{iso}}{\partial \overline{I}_2} \tag{4.6}$$

The derivative of volumetric term is given as

$$\mathbf{S}_{vol} = 2\frac{\partial U}{\partial \mathbf{C}} = K\left(J^2 - 1\right)\mathbf{C}^{-1} \tag{4.7}$$

Another new anisotropic finite strain viscoelastic constitutive model was presented by Liu et al. [63], which was based on Holzapfel type anisotropic hyperelastic strain–energy function. In this model, the anisotropic viscous part was set as independent of the isotropic viscous part. Moreover, the modified elastic deformation gradient is expressed in fiber and matrix part as $\overline{\mathbf{F}}_{\mathrm{e}}^{\mathrm{f}} = J^{-1/3}\mathbf{F}_{\mathrm{e}}^{\mathrm{f}}$ and $\overline{\mathbf{F}}_{\mathrm{e}}^{\mathrm{m}} = J^{-1/3}\mathbf{F}_{\mathrm{e}}^{\mathrm{m}}$, respectively. For modified viscous deformation gradient, the subscript e is replaced by v. Similarly, the modified right Cauchy green tensor for the elastic and viscous parts of the matrix and the fiber is written as

$$\overline{\mathbf{C}}_{\mathrm{e}}^{\mathrm{m}} = \left(\overline{\mathbf{F}}_{\mathrm{e}}^{\mathrm{m}}\right)^{\mathrm{T}}\overline{\mathbf{F}}_{\mathrm{e}}^{\mathrm{m}} = J^{-2/3}\mathbf{C}_{\mathrm{e}}^{\mathrm{m}} \tag{4.8}$$

$$\overline{\mathbf{C}}_{\mathrm{e}}^{\mathrm{f}} = \left(\overline{\mathbf{F}}_{\mathrm{e}}^{\mathrm{f}}\right)^{\mathrm{T}}\overline{\mathbf{F}}_{\mathrm{e}}^{\mathrm{f}} = J^{-2/3}\mathbf{C}_{\mathrm{e}}^{\mathrm{f}} \tag{4.9}$$

$$\overline{\mathbf{C}}_{\mathrm{v}}^{\mathrm{m}} = \left(\overline{\mathbf{F}}_{\mathrm{v}}^{\mathrm{m}}\right)^{\mathrm{T}}\overline{\mathbf{F}}_{\mathrm{v}}^{\mathrm{m}} = J^{-2/3}\mathbf{C}_{\mathrm{v}}^{\mathrm{m}} \tag{4.10}$$

$$\overline{\mathbf{C}}_{\mathrm{v}}^{\mathrm{f}} = \left(\overline{\mathbf{F}}_{\mathrm{v}}^{\mathrm{f}}\right)^{\mathrm{T}}\overline{\mathbf{F}}_{\mathrm{v}}^{\mathrm{f}} = J^{-2/3}\mathbf{C}_{\mathrm{v}}^{\mathrm{f}} \tag{4.11}$$

The SEF is written in the article [63] as

$$
\begin{aligned}
\Psi(\overline{I}_1,\overline{I}_e,\overline{I}_4,\overline{I}_{4e},J) = \; & \underbrace{c(\overline{I}_1-3)}_{\text{isochoric–isotropic–equilibrium}} + \underbrace{\beta_1 c(\overline{I}_e-3)}_{\text{isochoric–isotropic–viscous}} \\
& + \underbrace{\begin{cases} \frac{k_1}{2k_2}\left[e^{k_2\left(\overline{I}_4-1\right)^2}-1\right] & \text{if} \quad I_4 \geq 1 \\ 0 & \text{if} \quad I_4 < 1 \end{cases}}_{\text{isochoric–anisotropic–equilibrium}} \\
& + \underbrace{\begin{cases} \beta_2\frac{k_1}{2k_2}\left[e^{k_2\left(\overline{I}_{4e}-1\right)^2}-1\right] & \text{if} \quad I_{4e} \geq 1 \\ 0 & \text{if} \quad I_{4e} < 1 \end{cases}}_{\text{isochoric–anisotropic–viscous}} \\
& + \underbrace{\frac{1}{2}\kappa(J-1)^2}_{\text{penalty–term}}.
\end{aligned}
\tag{4.12}
$$

and the modified invariants are described by

$$\overline{I}_1\left(\overline{\mathbf{C}}\right) = tr\left(\overline{\mathbf{C}}\right) \tag{4.13}$$

$$\overline{I}_e\left(\overline{\mathbf{C}}\right) = \mathbf{I} : \overline{\mathbf{C}}^{\mathrm{m}}_{\mathrm{e}} = \overline{\mathbf{C}} : \left(\mathbf{C}^{\mathrm{m}}_{\mathrm{v}}\right)^{-1} \tag{4.14}$$

$$\overline{I}_4\left(\overline{\mathbf{C}},\ \mathbf{a}_0\right) = \overline{\mathbf{C}} : \left(\mathbf{a}_0 \otimes \mathbf{a}_0\right) \tag{4.15}$$

$$\overline{I}_{4e}\left(\overline{\mathbf{C}},\ \mathbf{a}_{\mathrm{v}}\right) = \overline{\mathbf{C}}^{\mathrm{f}}_{\mathrm{e}} : \mathbf{a}_{\mathrm{v}} \otimes \mathbf{a}_{\mathrm{v}} \tag{4.16}$$

$$I_{4v}\left(\mathbf{C}\right) = \mathbf{C}^{\mathrm{f}}_{\mathrm{v}} : \left(\mathbf{a}_0 \otimes \mathbf{a}_0\right) \tag{4.17}$$

The viscous unit vector $\mathbf{a}_{\mathrm{v}}$ of the form $\mathbf{a}_{\mathrm{v}} = \frac{\mathbf{F}^{\mathrm{f}}_{\mathrm{v}}\mathbf{a}_0}{\left|\mathbf{F}^{\mathrm{f}}_{\mathrm{v}}\mathbf{a}_0\right|}$ and the elastic fiber $\overline{I}_{4e}$ is written in the article as $\frac{\overline{I}_4}{I_{4v}}$. In Eq. (4.14), the only trickiest part is to calculate the modified right Cauchy green tensor for the viscous part of the matrix $(\mathbf{C}^{\mathrm{m}}_{\mathrm{v}})$. This is detailed in the integration algorithm for the evolution equation of the isotropic viscous part in [63]. The derivative of these modified invariants for the second Piola–Kirchhoff stress tensor ($\mathbf{S}$) is defined in the article by

$$\overline{\mathbf{S}} = 2\frac{\partial\overline{\psi}}{\partial *}\frac{\partial *}{\partial\overline{\mathbf{C}}} : \frac{\partial\overline{\mathbf{C}}}{\partial\mathbf{C}} \tag{4.18}$$

where *'s are the modified invariants used in Eq. 4.12.

4.2 Material Models and Methods

The geometric model of the human prostate used in this section is shown in Fig. 4.2. It is the realistic model obtained from BodyParts3D database [70]. As described in Chap. 3, the geometry of the prostate is concurrent with the experimental data in the Johnson et al. [55] article; the total volume of the prostate is 28064 mm^2, and the height is 31.7 mm. In this section, we reproduce the results by using the probing technique given in the article; a probe with a flat circular (4.9 mm diameter) force is applied inward to the prostate at a strain rate 25%. To simulate the behavior of prostate, it is necessary to consider the fiber direction described in Sinha et al. [103] which in our case in Z–direction of prostate geometry. In this thesis, we propose a new constitutive model for the anisotropic–viscoelastic behavior of the prostate geometry by following the models presented by Tuset et al. [113] and Liu et al. [63].

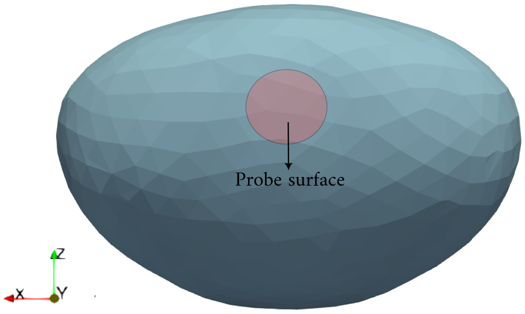

Figure 4.2: Coronal plane of a human prostate geometry.

4.2.1 New Constitutive Model

We followed the trend observed in two different literature [63, 113]. We first replace the isochoric–isotropic–equilibrium part of Eq. 4.12 by the isotropic part of Eq. 4.1, which involves two constants (C_1 and C_2). Then we replace the isochoric–isotropic–viscous part in Eq. 4.12 with the quadratic polynomial of modified elastic invariants ($\bar{I}_e$), involving the same two constants C_1 and C_2. After that, we replace the equilibrium and viscous part isochoric–anisotropic terms in Eq. 4.12 with the bi-quadratic polynomial function of modified fiber ($\overline{I}_4$), described in Eq. 4.1 (fiber–part) and elastic invariants of the modified fiber ($\overline{I}_{4e}$), respectively. Both new polynomial functions involve two more constants C_3 and C_4. The final form of the modified strain energy function (SEF), along with the independence of equilibrium and viscous parts, are defined as

$$\begin{aligned}
\overline{\psi}\left(\overline{I}_1,\, \overline{I}_e,\, \overline{I}_4,\, \overline{I}_{4e},\, J\right) = & \underbrace{C_1\left(\overline{I}_1 - 3\right) + C_2\left(\overline{I}_1 - 3\right)^2}_{\text{isochoric–isotropic–equilibrium}} \\
& + \underbrace{\beta_1\left(C_1(\overline{I}_e - 3\right)^2 + C_2\left(\overline{I}_e - 3)^2\right)}_{\text{isochoric–isotropic–viscous}} \\
& + \underbrace{C_3\left(\overline{I}_4 - 1\right)^2 + C_4\left(\overline{I}_4 - 1\right)^4}_{\text{isochoric–anisotropic–equilibrium}} \\
& + \underbrace{\beta_2\left(C_3(\overline{I}_{4e} - 1)^2 + C_4\left(\overline{I}_{4e} - 1\right)^4\right)}_{\text{isochoric–anisotropic–viscous}} \\
& + \underbrace{\frac{1}{2}K\left(J^2 - 1 - 2\ln J\right)}_{\text{volumetric part}}
\end{aligned} \tag{4.19}$$

where C_i, $i = 1, 2, 3$ and 4 are positive constants. K is the bulk modulus that can be adjusted for the incompressible response. β_1 and β_2 are the positive non-dimensional proportional factor for the isotropic and anisotropic viscous parts, respectively. The volumetric part of SEF in (4.19) is the same as in [113], which was first described by Simo and Miehe's [99]. We can write the SEF (Eq. (4.19)) in compact form as

$$\overline{\psi}\left(J,\, \overline{\mathbf{C}}\right) = \overline{\psi}_{eq}^{iso} + \overline{\psi}_{vis}^{iso} + \overline{\psi}_{eq}^{ani} + \overline{\psi}_{vis}^{ani} + \psi_{vol} \tag{4.20}$$

We considered one family of fibers to investigate viscoelasticity. The direction of fiber in reference configuration is defined by the unit vector a_0 with $|a_0| = 1$. The second Piola–Kirchhoff stress tensor ($\mathbf{S}$) comes from the derivative of SEF (4.20) formulation proposed in this thesis chapter as

$$\overline{\mathbf{S}} = 2\frac{\partial\overline{\psi}}{\partial\mathbf{C}} = \overline{\mathbf{S}}_{\mathrm{eq}}^{\mathrm{iso}} + \overline{\mathbf{S}}_{\mathrm{vis}}^{\mathrm{iso}} + \overline{\mathbf{S}}_{\mathrm{eq}}^{\mathrm{ani}} + \overline{\mathbf{S}}_{\mathrm{vis}}^{\mathrm{ani}} \tag{4.21}$$

The volumetric part second of Piola–Kirchhoff stress tensor ($\mathbf{S}$) is represented by $\mathbf{S}_{\mathrm{vol}}$. The derivative $\frac{\partial \overline{\mathbf{C}}}{\partial \mathbf{C}}$ from Holzapfel [48] are used in the subsequent analysis and introduced in [113], i.e.

$$\mathbb{P}(J, \mathbf{C}) = \frac{\partial \overline{\mathbf{C}}}{\partial \mathbf{C}} = J^{-\frac{2}{3}} \left(\mathbf{I} - \frac{1}{3} \mathbf{C} \otimes \mathbf{C}^{-1} \right) \tag{4.22}$$

Here, $\mathbf{I}$ is symmetric 4th order tensor. Using the Eq. 4.22 and derivative in Eq. 4.18, we find the derivatives of each isochoric term in Eq. 4.20 by

$$\begin{aligned} \overline{\mathbf{S}} = \overline{\gamma}_1 J^{-\frac{2}{3}} \left(\mathbf{I} - \frac{1}{3} I_1 \mathbf{C}^{-1} \right) + \overline{\gamma}_2 J^{-\frac{2}{3}} \left((\mathbf{C}_{\mathrm{v}}^{\mathrm{m}})^{-1} - \frac{1}{3} \left[\mathbf{C} : (\mathbf{C}_{\mathrm{v}}^{\mathrm{m}})^{-1} \right] \mathbf{C}^{-1} \right) \\ + \overline{\gamma}_3 \overline{I}_4 J^{-\frac{2}{3}} \left(\frac{\mathbf{a}_0 \otimes \mathbf{a}_0}{\overline{I}_4} - \frac{1}{3} \overline{\mathbf{C}}^{-1} \right) + \overline{\gamma}_4 \overline{I}_{4\mathrm{e}} J^{-\frac{2}{3}} \left(\frac{\mathbf{a}_0 \otimes \mathbf{a}_0}{\overline{I}_4} - \frac{1}{3} \overline{\mathbf{C}}^{-1} \right) \end{aligned} \tag{4.23}$$

$$\overline{\gamma}_1 = 2 \frac{\partial \overline{\psi}_{eq}^{iso}}{\partial \overline{I}_1} = 2C_1 + 4C_2 \left(\overline{I}_1 - 3 \right) \tag{4.24}$$

$$\overline{\gamma}_2 = 2 \frac{\partial \overline{\psi}_{vis}^{iso}}{\partial \overline{I}_e} = 2\beta_1 \left(C_1 + 4C_2 \left(\overline{I}_e - 3 \right) \right) \tag{4.25}$$

$$\overline{\gamma}_3 = 2 \frac{\partial \overline{\psi}_{eq}^{ani}}{\partial \overline{I}_4} = 4 \left(\overline{I}_4 - 1 \right) \left(C_3 + 2C_4 \left(\overline{I}_4 - 1 \right)^2 \right) \tag{4.26}$$

$$\overline{\gamma}_4 = 2 \frac{\partial \overline{\psi}_{vis}^{ani}}{\partial \overline{I}_{4e}} = 4 \left(\overline{I}_{4e} - 1 \right) \left(C_3 + 2C_4 \left(\overline{I}_{4e} - 1 \right)^2 \right) \tag{4.27}$$

The volumetric part of stress tensor ($\mathbf{S}$) is given by

$$\mathbf{S}_{\mathrm{vol}} = \overline{\gamma}_5 \mathbf{C}^{-1} \tag{4.28}$$

$$\overline{\gamma}_5 = 2 \frac{\partial \overline{\psi}_{vol}}{\partial J} = 2K \left(J^2 - 1 \right) \tag{4.29}$$

In this thesis, we used the specific interface provided by the `MFront` software to incorporate this new constitutive model into the `Code_Aster`. The FE discretization approach of Simo and Miehe [99] is used for the Code Aster nonlinear solver, as it is effective for large deformations. In `Code_Aster`, the non–linear equations are solved by the Newton method, and the computation of the isochoric part of the fourth order tangent tensor, $\mathbb{E}$ has to be defined as

$$\mathbb{E} = \mathbb{E}_{iso} + \mathbb{E}_{vol} \tag{4.30}$$

$$\mathbb{E}_{iso} = \frac{\partial \overline{\mathbf{S}}}{\partial \mathbf{C}} = \overline{\mathbb{E}}^{\text{iso}}_{\text{eq}} + \overline{\mathbb{E}}^{\text{iso}}_{\text{vis}} + \overline{\mathbb{E}}^{\text{ani}}_{\text{eq}} + \overline{\mathbb{E}}^{\text{ani}}_{\text{vis}} \tag{4.31}$$

The contribution of the volumetric part $\mathbb{E}_{\text{vol}}$ is given by,

$$\mathbb{E}_{\text{vol}} = \frac{\partial \overline{\mathbf{S}}_{vol}}{\partial \mathbf{C}} = KJ^2\mathbf{C}^{-1} \odot \mathbf{C}^{-1} - K\left(J^2 - 1\right)\mathbf{C}^{-1} \otimes \mathbf{C}^{-1} \tag{4.32}$$

The following identity given in [113] can be used in practice to avoid the expensive calculations of the double contraction of the isochoric part of $\overline{\mathbf{S}}$ and $\mathbb{P}$, such as

$$\overline{\mathbf{S}} : \mathbb{P} = J^{-\frac{2}{3}}\left(\overline{\mathbf{S}} - \frac{1}{3}\left(\overline{\mathbf{S}} : \mathbf{C}\right)\mathbf{C}^{-1}\right) \tag{4.33}$$

We followed the contribution to the isochoric part involved in [113] as:

$$\begin{aligned}\mathbb{E}_{iso} &= \mathbb{P}^{\mathrm{T}} : \overline{\mathbb{E}} : \mathbb{P} - \frac{1}{3}J^{-\frac{2}{3}}\left(\overline{\mathbf{S}} \otimes \mathbf{C}^{-1} + \mathbf{C}^{-1} \otimes \overline{\mathbf{S}}\right) \\ &+ \frac{1}{3}\left(\overline{\mathbf{S}} : \overline{\mathbf{C}}\right)\left(\mathbf{C}^{-1} \odot \mathbf{C}^{-1} + \frac{1}{3}\mathbf{C}^{-1} \otimes \mathbf{C}^{-1}\right)\end{aligned} \tag{4.34}$$

We wrote the non-standard circledot($\odot$) function in C++, and it is included in the code. It executes the tensor operation $\mathbf{C}^{-1} \odot \mathbf{C}^{-1}$ = -$\frac{\partial \mathbf{C}^{-1}}{\partial \mathbf{C}}$ using the following equivalences [48] also mentioned in [113], i.e.

$$\begin{aligned}&\mathbf{I} = \mathbf{C}^{-1}\mathbf{C} \\ &\mathbb{O} = \frac{\partial \mathbf{C}^{-1}}{\partial \mathbf{C}}\mathbf{C} + \frac{\partial \mathbf{C}}{\partial \mathbf{C}} = \frac{\partial \mathbf{C}^{-1}}{\partial \mathbf{C}}\mathbf{C} + \mathbb{I}^s \\ &\frac{\partial \mathbf{C}^{-1}}{\partial \mathbf{C}} = -\mathbf{C}^{-1}\mathbb{I}^s\mathbf{C}^{-1} = -\mathbf{C}^{-1} \odot \mathbf{C}^{-1}\end{aligned} \tag{4.35}$$

$\mathbb{I}^s$ stands for a specific symmetric form of the fourth order identity tensor in equation 4.35. The calculation of $\mathbb{P}^{\mathrm{T}} : \overline{\mathbb{E}} : \mathbb{P}$ presented as

$$
\begin{aligned}
\mathbb{P}^{\mathrm{T}} : \overline{\mathbb{E}} : \mathbb{P} = {} & \frac{1}{9}\left(4C_2\bar{I}_1^2 + 4\beta_1 C_2 \bar{I}_e^2 + 4C_3 + 24C_4(\bar{I}_4 - 1)^2\bar{I}_4^2\right)\left(\mathbf{C}^{-1} \otimes \mathbf{C}^{-1}\right) \\
& + \frac{\bar{I}_{4e}^2}{9I_{4v}}\beta_2\left(4C_3 + 24C_4(\bar{I}_{4e} - 1)^2\right)\left(\mathbf{C}^{-1} \otimes \mathbf{C}^{-1}\right) \\
& + \left(4C_2 J^{-\frac{4}{3}}\right)(\mathbf{I} \otimes \mathbf{I}) + \left(4C_2\beta_1 J^{-\frac{4}{3}}\right)\left(\mathbf{C}_{\mathrm{v}}^{\mathrm{m}} \otimes \mathbf{C}_{\mathrm{v}}^{\mathrm{m}}\right) \\
& + J^{-\frac{4}{3}}\left(4C_3 + 24C_4(\bar{I}_4 - 1)^2 + \frac{\beta_2}{I_{4v}}\left(4C_3 + 24C_4(\bar{I}_{4e} - 1)^2\right)\right)(\mathbf{a}_0 \otimes \mathbf{a}_0) \\
& - \frac{1}{3}\left(4C_2 J^{-\frac{2}{3}}\bar{I}_1\right)\left(\left(\mathbf{I} \otimes \mathbf{C}^{-1}\right) + \left(\mathbf{C}^{-1} \otimes \mathbf{I}\right)\right) \\
& - \frac{1}{3}\left(4\beta_1 C_2 J^{-\frac{2}{3}}\bar{I}_e\right)\left(\left(\mathbf{C}_{\mathrm{v}}^{\mathrm{m}} \otimes \mathbf{C}^{-1}\right) + \left(\mathbf{C}^{-1} \otimes \mathbf{C}_{\mathrm{v}}^{\mathrm{m}}\right)\right) \\
& - \frac{1}{3}J^{-\frac{2}{3}}\bar{I}_4\left(4C_3 + 24C_4(\bar{I}_4 - 1)^2 + \frac{\beta_2}{I_{4v}}\left(4C_3 + 24C_4(\bar{I}_{4e} - 1)^2\right)\right) \\
& \left(\left(\mathbf{a}_0 \otimes \mathbf{C}^{-1}\right) + \left(\mathbf{C}^{-1} \otimes \mathbf{a}_0\right)\right)
\end{aligned}
\tag{4.36}
$$

We implemented this new constitutive model as a user-supplied code provided by `MFront` software to incorporate into the `Code_Aster`. The user-supplied code is given the gradient tensor $\mathbf{F}$ as an input parameter and returns the estimated values of $\mathbf{S}$ or σ and $\mathbb{E}$ on exit. The most appealing aspect of `MFront` is its elegant high-level language, which is particularly well suited for tensor algebra and its simple integration with `Code_Aster`. Therefore, in the Appendix section of this thesis, we provided the detailed codes of `Code_Aster` and `MFront` of our new constitutive model.

4.3 Result and Discussion

Prostate tissue geometry is characterized by the new constitutive model described in the above section. We used general approach to determine the constants (K, C_1, C_2, C_3, C_4, β_1, β_2, τ_1 and τ_2) involved by using trial and error approach that best fitted the experimental data of prostate (available in literature [55]). We fixed one end of prostate geometry (-Y side) and the opposite end (+Y) is compressed inwards into the -Y direction, similar to the probing technique given in the article [55]. The fibers are aligned in the Z–direction of the prostate geometry.

The displacement boundary conditions are used in our dynamical model to obtain stress–strain curve close to the experimental curve. We used the maximum strain value of 0.271, which we extracted from experimental data at a strain rate 25%. Moreover, the representative stress–strain curve is illustrated in Fig. 4.3, in which the maximum stress value is 0.052 MPa.

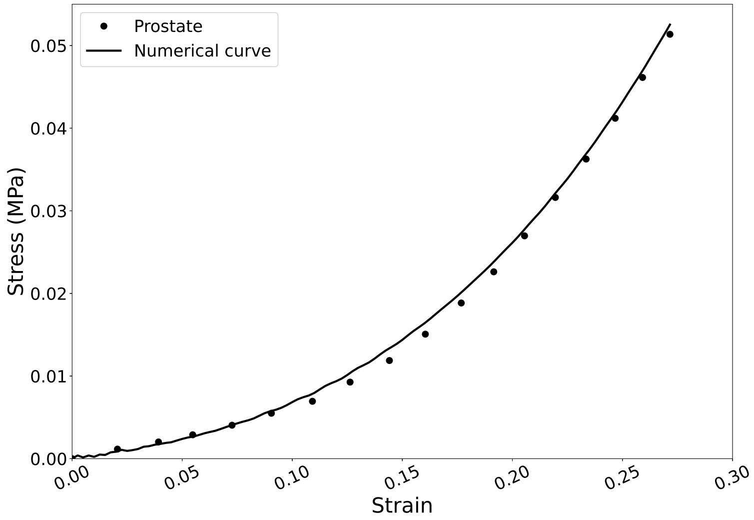

Figure 4.3: Fitting of human prostate geometry with the new anisotropic–viscoelastic constitutive model. Curve with line show numerical result.

The material parameters used in the constitutive model reproducing the experimental prostate data are summarized in Table 4.1. The parameters τ_1 and τ_2 come from the integration of the evolution equation while calculating the inverse of modified right Cauchy green tensor for the viscous part of the matrix $(\mathbf{C}_{\mathrm{v}}^{\mathrm{m}})$ [63]. Figure 4.4 shows the simulation results in coronal, sagittal and axial views. The maximum displacement of 8.6 mm is obtained when the prostate is probed at one end. As a result, the prostate also expanded along X–direction.

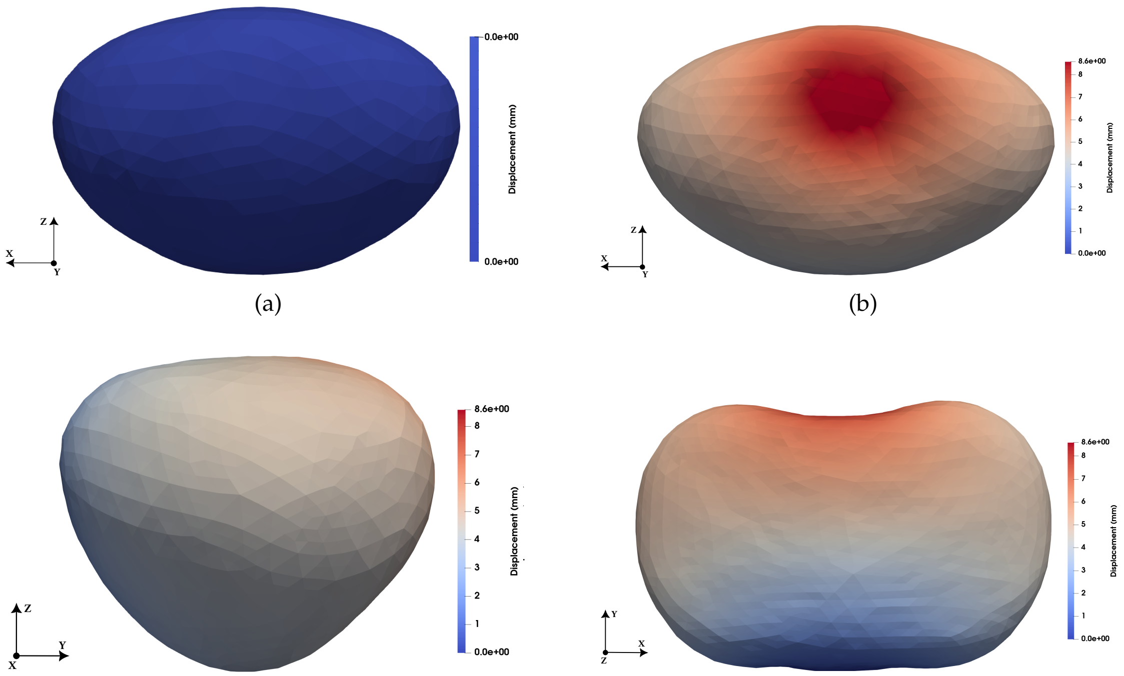

(a) (b)

(c) (d)

Figure 4.4: Undeformed (a) and deformed (b) prostate geometry in coronal view, sagittal view (c) and axial view (d).

Table 4.1: Values of the material coefficients used in the constitutive model (3.11) that produce the best fitting to experimental data for human prostate.

Parameter	K(MPa)	C_1(MPa)	C_2(MPa)	C_3(MPa)	C_4(MPa)	β_1	β_2	τ_1	τ_2
3D formulation	1	0.000043	0.00091	0.00027	0.00031	0.5	0.5	2.5	2.5

4.4 Conclusions

In this chapter, we proposed a new anisotropic–viscoelastic constitutive model to characterize the mechanical properties of the human prostate gland. The present model can easily be used to simulate the problems in which the whole geometry is being compressed with strain (ϵ) level up to 0.27. We also tried to simulate the prostate geometry using the models given in [113, 63], but could not obtain the resulting prostate deformation under the probing technique. In this regard, we can say that the new constitutive model using the polynomial functions of invariants is more numerically stable. However, we need further experimental data on the human prostate, like hysteretic characteristics and relaxation effects, to authenticate our model, which can be used for clinical applications in the future.

Chapter 5

Concluding Remarks

This final chapter presents the most important contributions and main conclusions of this dissertation, emphasizing their significance. In addition, the chapter also includes approaches for future work.

5.1 Thesis highlights

The main contribution of this thesis work is to trace the location of prostate lesions during the biopsy. We achieved this work with the following significant aspects. Firstly, the accurate and realistic 3-D male pelvis model is presented after the intersection of meshes between the pelvis organs and bones is conveniently refined and modified (removed undesirable intersections of adjacent elements). Then we applied linear elastic properties to the pelvis organs for the biomechanical simulation when TRUS beam pressure was applied at the rectum wall. Our results revealed that the 30N force exerted by the TRUS probe on the rectum wall led to a significant motion and deformation of the prostate. The PI-RAIDS map and superimposition of slices using the registration technique provided an extra layer of knowledge about the prostate neoplasms location.

Secondly, this research work concerns the applicability of the biomechanical pelvis model to understand the mechanical circumstances of several normal and pathological scenarios in the prostate and during the biopsy. For this, we applied non-linear properties of soft tissues except vesical muscles to the multi-constituent Signorini model to see the overall deformation of the pelvis model, mainly of the prostate and its lesions location. Our results revealed that the deformations of pelvis organs that come from the non–linear model are less than those obtained in the linear model. Similarly, the displacement of prostate lesions in the linear elastic model ranged between 5.20 and 13.93 mm, whereas the hyperelastic model ranged from 5.35 to 11.12 mm. The differences in the values are due to the stiff material properties of the prostate. Also, we know that soft biological tissues are often characterized by highly non–linear mechanical behavior, which works for large strains. But, in our case, the resulting deformation of organs is less with a 30 N biopsy force at the rectum wall.

Besides, we proposed our new constitutive model for the prostate's anisotropic–viscoelastic behavior. The new model is independent of anisotropic and viscoelastic parts, which are based on polynomial functions of certain invariants quantities. The material parameters for the constitutive model provide stress–strain results that fit well with the experimental data. Our new constitutive model can be important to characterize all the mechanical properties of the prostate gland, especially under probing/compression scenarios, because knowing the properties of the prostate will allow the researcher to better understand the mechanism of injury under traumatic situations.

5.2 Future research lines

The work explained in this thesis and the obtained results predict future research lines. Unfortunately, some predictions were omitted from the thesis due to time restrictions and lack of experimental data.

We will consider the complete zones of the prostate and the volumes of pelvis organs for the simulations of the pelvis model. This is important to understand how much bladder and rectum volume affects the prostate lesions location during the biopsy. Moreover, prostate deformation induced by the transrectal needle will also consider for future work. There is a lack of experimental data on soft tissues of the pelvis model. If we find the mechanical properties, we will include them in the simulation of the pelvis model for more accurate estimates of prostate neoplasms displacement.

The mechanical properties of the prostate gland are essential for clinicians to diagnose better prostate-related problems and injury prevention, like how much force threshold is required before rupturing during operations/clinical findings. Therefore we will obtain the mechanical properties considering the hysteretic characteristics of prostate and relaxations effects if we find the related experimental data.

Appendix A

MFront and Code_Aster Pseudocodes

This section describes implementing a new constitutive anisotropic–viscoelastic model in `Code_Aster` open source software and `MFront` codes [36, 45]. MFront is a code generation tool covering three material knowledge types: material properties, mechanical behaviors and a simple point-wise model. For clarity, we explained the implementations of pseudocodes step by step i.e.; the descriptions are provided under each box–code.

A.1 MFront Implementation

A.1.1 Description of the MFront implementation

```
@DSL DefaultFiniteStrain;
@ModellingHypothesis Tridimensional;
@Author MedSim;
@Behaviour liuprot;
@Date 02/02/2022;
@Description {Transversely Isotropic
              Visco-Hyperelastic Behaviour}
@Includes {#include "../circledot_Hzpf-Prot-Tuset.h" }
```

The first keyword, "@DSL" is a domain-specific language and the behavior "DefaultFiniteStrain" does not restrict the integration method's behavior. The keyword "@ModellingHypothesis Tridimensional" allows the user to choose the modeling hypothesis; in our case, it is Tridimensional which is 3D. In case of strain, we have EXX, EYY, EZZ, EXY, EXZ and EYZ. The other keywords: "Author, Behavior, Date and Description" are the names given by the user. Finally, the "@Includes" keyword is the external location of file where we implemented the hand-made matrix notation for symmetric matrix.

A.1.2 Association of Material Property to a Material

```
@MaterialProperty   real K;
@MaterialProperty   real C1, C2, C3, C4, beta1, beta2, tau1, tau2;
@MaterialProperty   real nx, ny, nz;
@LocalVariable   real J, iJb, constv, UpJ, I1b, I4b, delta1, deltae,
                 delta4, delta4e, Ieb, I4eb, I4v;
@LocalVariable   Stensor id, C, C_inv, C_bar, n0n0, Cmv_inv;
@LocalVariable   StressStensor S_bar;
@LocalVariable   size_t index;
@InitLocalVariables{
I4eb = 1.0;
index = 0;
}
@LocalVariable StiffnessTensor dS_dC;
```

In this part, we define the material properties like constants involved in the constitutive model and the direction of fibers in terms of unit vector; nx, ny and nz. Similarly, the invariants, stress tensor, Cauchy stress and others are defined with the @LocalVariable to store the consistent tangent operator $\frac{d\mathbf{S}}{d\mathbf{C}}$.

A.1.3 Computation of the right Cauchy tensor C, the invariants and the invariants derivatives

```
@Integrator{
id = Stensor::Id();
J = det(F1);
C = computeRightCauchyGreenTensor(F1);
C_inv = invert(C);
iJb = pow(J, -2.0/3.0);
C_bar = iJb*C;
tvector<3u, real> n0{nx, ny, nz};
n0n0 = Stensor::buildFromVectorDiadicProduct(n0);
/* update I4eb value (Newton iteration) */
index = counter(1.0e-05, C3, C4, tau2); // must be invoked prior to
          the update_I4eb() call
I1b = trace(C_bar);
I4b = C_bar | n0n0;
I4eb = update_I4eb(F0, I4b, dt, tau2, C3, C4);
I4v = get_I4v(); // invoke after the update_I4eb() call
Cmv_inv = update_Cmv(C_inv, dt, tau1, 1.0); //invoke after the
             update_I4eb() call
Ieb = C_bar | Cmv_inv;
```

In this section, we calculate variables like identity tensor, invariants, modified invariants, right Cauchy green tensor **C**, the initial orientation of unit vector for fiber and the derivatives of the invariants. We use the @integrator operator to update the auxiliary state variables. The keyword "Stensor" represents the symmetric tensor. The inverse of the right Cauchy green tensor for the viscous part of the matrix ($(\mathbf{C}_{\mathrm{v}}^{\mathrm{m}})^{-1}$) is provided. In this code, we used the Integration algorithm for the evolution equation of the isotropic viscous part from the Liu et al. [63] article for the calculation of $(\mathbf{C}_{\mathrm{v}}^{\mathrm{m}})^{-1}$. The contraction operator (:) is written as a vertical bar (|) in `MFront` code.

A.1.4 Computation of the Isochoric Part of the Second Piola–Kirchhoff Stress

```
double  gamma1{2.0*C1 + 4.0*C2*(I1b - 3.0)};
double  gammae{beta1*(2.0*C1 + 4.0*C2*(Ieb - 3.0))};
double  gamma4{4.0*C3*(I4b - 1.0) + 8.0*C4*pow(I4b - 1.0, 3)};
double  gamma4e{beta2*(4.0*C3*(I4eb - 1.0) +
                    8.0*C4*pow(I4eb - 1.0, 3))/I4v};
delta1 = 4.0*C2;
deltae = beta1*delta1;
delta4 = 4.0*C3 + 24.0*C4*(I4b - 1.0)*(I4b - 1.0);
delta4e = beta2*(4.0*C3 + 24.0*C4*(I4eb - 1.0)*(I4eb - 1.0))/          (I4v*I4v);
/* isochoric part (fiber term included) */
S_bar = gamma1*id + gammae*Cmv_inv + (gamma4 +
          gamma4e)*n0n0;
const  double  const2{(S_bar | C)/3.0};
StressStensor  S_iso{iJb*(S_bar - const2*C_inv)};
```

The calculation of the isochoric part of the second Piola–Kirchhoff stress tensor **S** (4.21) is described. For our simplicity, we divided the equation into different parts.

A.1.5 Computation of the Volumetric Part of the Second Piola–Kirchhoff Stress

```
UpJ = K*(J*J - 1.0);
constv = K*J*J;
StressStensor  Sv{UpJ*C_inv};
```

Here, we compute the volumetric part of the second Piola–Kirchhoff stress tensor.

A.1.6 Computation of the Cauchy stress

```
sig = convertSecondPiolaKirchhoffStressToCauchyStress(Sv +          S_iso, F1) ;}
```

To finish the calculation of the second Piola–Kirchhoff stress tensor **S**, it is necessary to include this function that converts the second tensor of Piola–Kirchhoff stress with the Cauchy stress tensor through the deformation gradient $\mathbf{F}_1$.

A.1.7 Computation of the Consistent Tangent Operator

```
@TangentOperator<DS_DC>{
```

The last part of the code is calculating the consistent tangent operator. But, first, it is necessary to calculate the isochoric and volumetric parts of the consistent tangent operator.

A.1.8 Computation of the Derivative of the Inverse Right Cauchy Green Tensor

```
Stensor4  C_inv_C_inv{C_inv^C_inv};
Stensor4  C_inv_cd_C_inv{circledot<N>(C_inv)};
```

As **C** is symmetric tensor and following definitions for the derivative of $\mathbf{C}^{-1}$ can be used:

$$-\frac{\partial \mathbf{C}^{-1}}{\partial \mathbf{C}} = \mathbf{C}^{-1} \odot \mathbf{C}^{-1}$$

$$\left(\mathbf{C}^{-1} \odot \mathbf{C}^{-1}\right)_{ijkl} = \left(\mathbf{C}^{-1}\right)_{ij} \left(\mathbf{C}^{-1}\right)_{kl}$$

The operator hat (^) in the code means Hadamard Product that is used to calculate element wise multiplication in a matrix.

A.1.9 Computation of the Volumetric Part of the Consistent Tangent Operator

```
Stensor4  E_vol{constv*C_inv_C_inv - UpJ*C_inv_cd_C_inv};
```

In this part, we compute the volumetric part of the consistent tangent operator.

A.1.10 Computation of the Isochoric Part of the Consistent Tangent Operator

```
/* isochoric part (with only the I4b terms into the fiber contribution)*/
double   const3{(delta1*I1b*I1b + deltae*Ieb*Ieb + elta4*I4b*I4b +
                  delta4e*I4eb*I4eb)/9.0};
Stensor4   PTEP {const3*C_inv_C_inv +
                  (delta1*iJb*iJb)*(id ˆ id) +
                  (deltae*iJb*iJb)*(Cmv_inv ˆ Cmv_inv) +
                  ((delta4+delta4e)*iJb*iJb)*(n0n0 ˆ n0n0) -
                  (delta1*I1b*iJb)/3.0*((idˆC_inv) + (C_invˆid)) -
                  (deltae*Ieb*iJb)/3.0*((Cmv_invˆC_inv) +
                  (C_invˆCmv_inv)) -
                  ((delta4 + delta4e)*I4b*iJb)/3.0*((n0n0ˆC_inv) +
                  (C_invˆn0n0))};
                  Stensor4   E_iso{PTEP -
                  (iJb/3.0)*((S_barˆC_inv) + (C_invˆS_bar)) +
                  (S_bar | C_bar)/3.0*(C_inv_cd_C_inv +
                  (1./3.)*C_inv_C_inv)} ;
```

The computation of the isochoric part of the consistent tangent operator is described. For the sake of clarity, we split the isochoric equation into different parts.

A.1.11 Computation of the Consistent Tangent Operator

```
dS_dC = E_vol + E_iso;
Dt = dS_dC;}
```

In the end, we obtain the consistent tangent operator.

The next step is to compile the .mfront (extension of mfront file) file and the compilation process generates two folders; include and src. In the src folder, we have a dynamic library "libAsterBehaviour.so" which must be coupled with the model generated in Code_Aster.

A.2 Code_Aster Implementation

The extension of the Code_Aster file is .comm and it begins with the variables involved throughout the problem. The explanation of the code is detailed below the box–code.

A.2.1 Read and Modify the Mesh

```
DEBUT()
MAIL = LIRE_MAILLAGE(FORMAT = ’MED’,
                     UNITE = 20)
                     MAIL = MODI_MAILLAGE(
                            reuse = MAIL,
                            MAILLAGE = MAIL,
                            ORIE_PEAU_3D = _F(
                            GROUP_MA =
                             (’fix’, ’force_face’)))
```

It begins with the keyword "LIRE_MAILLAGE" which means read the mesh which is assigned the Fortran unit LU 20 (Logical Unit 20) by default. The "MODI_MAILLAGE" means to modify the mesh to avoid errors, especially in the case of 3D studies. Finally, the keyword "ORIE_PEAU_3D" reorientate meshes of edges so that their normals are coherent. It is important if one wants to apply pressure to the skin. For example, the part of prostate meshes ’force_face’ and ’fix’ in our case.

A.2.2 Making a FEM from the Mesh

```
MODE = AFFE_MODELE(AFFE = _F(MODELISATION=’3D’,
                             PHENOMENE =
                             ’MECANIQUE’,
                             TOUT = ’OUI’),
                             MAILLAGE = MAIL)
```

Here, we define the physical phenomenon like in our case is ′MECHANIQUE′ (associated conservation equation) and type of finite element which is ′3–D′ in the code. The keywords "TOUT" and "OUI" means ′all′ and ′yes′.

A.2.3 Defining a Material Properties

```
mater = DEFI_MATERIAU(ELAS=_F(E=Young,
                              NU = NU,
                              RHO =  DENS),
                             MFRONT =  _F(LISTE_COEF
                              = (K, k1, k2, c, beta1, beta2,
                              tau1, tau2, nx, ny, nz)))
```

In this part, we define the material properties. As we are performing the non–linear dynamical analysis and we need the elastic modulus (E), Poisson ratio (ν) and rho density (ρ) values in our code, along with the list of variables involved in our constitutive model which is described in the above section of `MFront` implementation.

A.2.4 Assigning Material Properties to the Elements

```
MATE =  AFFE_MATERIAU(AFFE = _F(MATER = (mater),
                                TOUT=  ′OUI′),
                                MAILLAGE =  MAIL)
```

Here we assign the material properties ′mater′ to the prostate elements groups.

A.2.5 Stepping for the solution

```
TPS =  DEFI_LIST_REEL(DEBUT=0.0,
INTERVALLE = _F(JUSQU_A = FiTime,
                      PAS=  0.01))
llista =  DEFI_LIST_INST(DEFI_LIST = _F(LIST_INST=TPS,
                                        PAS_MAXI = 0.01,
                                        PAS_MINI = 1e-10),
                                        METHODE =  'AUTO')
```

This part involves time step. The keyword "PAS" means we divide the time step with a difference of 0.01. Let's suppose in the non–linear analysis that if the Newton method does not converge at a one-time step, it automatically reduces the time step with "PAS_MINI" function. Also, in the post-processing, we see our simulation results with an interval of time steps listed in "TPS" function.

A.2.6 Fixed Boundary Condition

```
formule0 = FORMULE(NOM_PARA='INST',
                        VALE= '(0.0)')
```

We define the fixed boundary condition at all time steps.

A.2.7 Step Function for Boundary Condition

```
FiTime = MaxStrain/StrainRate
def  step(x):
        if x <= FiTime:
            return -(MaxStrain*Depth)*x/FiTime
        else:
            return -(MaxStrain*Depth);
deplm = FORMULE(NOM_PARA = ('X', 'Y', 'Z', 'INST'),
                        VALE =  'step(INST)',
                        step = step)
```

Here, the step function is provided for the dynamical analysis. As we are doing the simulations of anisotropic–viscoelastic behavior of the prostate, we applied displacement boundary conditions.

A.2.8 Defining boundary conditions

```
grav1 = AFFE_CHAR_MECA_F(DDL_IMPO=(_F(DX= formule0,
                                        DY = formule0,
                                        DZ = formule0,
                         GROUP_NO=('node_fix')),
                         FORCE_FACE = _F(DY=deplm,
                         DX=formule0, DZ=formule0,
                         GROUP_NO= ('depl_nodes'),
                         MODELE = MODE)
```

We define the boundary conditions with Keyword "AFFE_CHAR_MECA_F". The Keyword "DDL_IMPO" is the degree of freedom (DOF) which we want to fix the mesh nodes. In this case, DX, DY and DZ is the displacement value in each of these directions in the global reference of the mesh definition. The keyword "FORCE_FACE" represents the nodes of a mesh where we want to apply the force/load.

A.2.9 Solving a Problem

```
RESU = DYNA_NON_LINE(ARCHIVAGE=_F(LIST_INST = TPS),
                     CHAM_MATER = MATE,
                     COMPORTEMENT = _F(
                     DEFORMATION = ’SIMO_MIEHE’,
                     LIBRAIRIE = ’/home/qasim/...
                     /src/libAsterBehaviour.so’,
                     NOM_ROUTINE= ’asterliuprot’,
                     RELATION= ’MFRONT’),
                     CONVERGENCE = _F(
                     ITER_GLOB_MAXI = 50),
                     EXCIT = _F(CHARGE = grav1,
                     TYPE_CHARGE = ’SUIV’),
                     INCREMENT = _F(
                     LIST_INST = llista),
                     MODELE = MODE,
                     NEWTON = _F(
                     MATRICE = ’TANGENTE’,
                     PREDICTION = ’TANGENTE’,
                     REAC_ITER = 1,))
```

This is the main part of the code, to solve the problem. After defining the boundary conditions and material properties, we conduct a dynamical analysis for our calculation, as the anisotropic–viscoelastic constitutive mmodel is highly non–linear and depends on time. The keyword "DEFORMATION = ’SIMO_MIEHE’" is used for the large deformation and expressed in the current configuration. Since we work with the MFront environment and the dynamic library ’libAsterBehaviour.so’, which we created by compiling the MFront file, we indicate the full path of the library under keyword "LIBRAIRIE". The keyword "NOM_ROUTINE" allows us to specify the chosen behavior model. With the "CONVERGENCE" keyword, we define the maximum iteration to solve the problem at every moment. We solve the non–linearity of the equations with the Newton method and it is possible to use the type of matrices like tangent or elastic for the prediction and correction.

A.2.10 Calculating Results

```
RESU = CALC_CHAMP(reuse = RESU,
                  CONTRAINTE = (’SIGM_ELNO’,
                  ’SIGM_NOEU’, ’SIGM_ELGA’),
                   CRITERES = (’SIEQ_ELNO’,
                  ’SIEQ_NOEU’),
                   DEFORMATION = (’EPSG_ELNO’,
                   ’EPSG_NOEU’, ’EPSI_NOEU’),
                   FORCE = (’FORC_NODA’,
                  ’REAC_NODA’),
                   RESULTAT = RESU)
```

It is necessary to indicate the stress and deformation field for post–processing. Under the CALC_CHAMP parameter, we define the stress or displacement field which we wish to calculate on the nodes or elements. For example, "SIGM_ELNO" represents the stress field with the nodes by element. Similarly, *_ELGA and *_NOEU represent field at the Gauss point per element and field with nodes, respectively. The word "SIEQ" means the equivalent stresses we want to calculate and FORCE words are the type of forces we want to extract.

A.2.11 Printing Results for Graphical Viewing

```
IMPR_RESU(FORMAT = ’MED’,
          RESU = _F(NOM_CHAM = (’DEPL’,
          ’SIGM_NOEU’, ’EPSG_NOEU’),
          RESULTAT = RESU,
          TOUT = ’OUI’,
          TOUT_CMP = ’OUI’),
          UNITE = 80)
FIN()
```

Finally, the results we want to be displayed graphically in the Post-Processing or Paraviews modules of `Salome-Meca` are then placed in a .med file. We save the results in .rmed file which has a unit number 80.

Bibliography

[1] M. Abdelkhalek et al. "Hemosepermia after transrectal ultrasound-guided prostatic biopsy: A prospective study". In: *Urology Annals* 5.1 (2013), pp. 30–33.

[2] Firas Abdollah et al. "Trans-rectal versus trans-perineal saturation rebiopsy of the prostate: is there a difference in cancer detection rate?" In: *Urology* 77.4 (2011), pp. 921–925.

[3] American College of Radiology. *Prostate imaging reporting and data system (PI-RADS)*. https://www.acr.org/Clinical-Resources/Reporting-and-Data-Systems/PI-RADS. Accessed 25-Nov-2021. 2021.

[4] Benelli Andrea et al. "The Role of MRI-TRUS Fusion Biopsy in the Diagnosis of Clinical Significant Prostate Cancer (CsPca)". In: *Male Reproductive Health*. 2019.

[5] A. Anssari-Benam, D.L. Bader, and H.R.C. Screen. "A combined experimental and modelling approach to aortic valve viscoelasticity in tensile deformation". In: *Journal of Materials Science: Materials in Medicine* 22.2 (2011), pp. 253–262.

[6] Alejandro Asraldi. "Diagnosis of cancer of the prostate: biopsy by rectal route". In: *Urol. Cutan Rev.* 41 (1937), p. 421.

[7] A. Bharatha et al. "Evaluation of three-dimensional finite element-based deformable registration of pre- and intraoperative prostate imaging". In: *Medical Physics* 28.12 (2001), pp. 2551–2560.

[8] A. Bhattarai and M. Staat. "Modelling of Soft Connective Tissues to Investigate Female Pelvic Floor Dysfunctions". In: *Computational and Mathematical Methods in Medicine* 2018 (2018).

[9] J.E. Bischoff, E.M. Arruda, and K. Grosh. "A rheological network model for the continuum anisotropic and viscoelastic behavior of soft tissue". In: *Biomechanics and Modeling in Mechanobiology* 3.1 (2004), pp. 56–65.

[10] A. Bjartell et al. "Production of alpha-1-antichymotrypsin by PSA-containing cells of human prostate epithelium". In: *Urology* 42.5 (1993), pp. 502–510.

[11] Nigel Borley and Mark R Feneley. "Prostate cancer: diagnosis and staging". In: *Asian journal of andrology* 11.1 (2009), p. 74.

[12] M.B. Boubaker et al. "Predictive model of the prostate motion in the context of radiotherapy: A biomechanical approach relying on urodynamic data and mechanical testing". In: *Journal of the Mechanical Behavior of Biomedical Materials* 49 (2015), p. 30.

[13] F. Bray et al. "The ever-increasing importance of cancer as a leading cause of premature death worldwide". In: *Cancer* 127.16 (2021), pp. 3029–3030.

[14] K.K. Brock et al. "A multi-organ biomechanical model to analyze prostate deformation due to large deformation of the rectum". In: vol. 6143 I. 2006.

[15] R. Cao et al. "Tissue mimicking materials for the detection of prostate cancer using shear wave elastography: A validation study". In: *Medical Physics* 40.2 (2013).

[16] E.L. Carniel et al. "Characterization of the anisotropic mechanical behaviour of colonic tissues: Experimental activity and constitutive formulation". In: *Experimental Physiology* 99.5 (2014), pp. 759–771.

[17] CGAL. *The Computational Geometry Algorithms Library*. `http://www.cgal.org`. Accessed 07-May-2021. 2017.

[18] G. Chagnon, M. Rebouah, and D. Favier. "Hyperelastic Energy Densities for Soft Biological Tissues: A Review". In: *Journal of Elasticity* 120.2 (2015), pp. 129–160.

[19] X. Chai et al. "Finite element based bladder modeling for image-guided radiotherapy of bladder cancer". In: *Medical Physics* 38.1 (2011), pp. 142–150.

[20] P. Chantereau et al. "Mechanical properties of pelvic soft tissue of young women and impact of aging". In: *International Urogynecology Journal* 25.11 (2014), pp. 1547–1553.

[21] E. Checcucci et al. "Artificial intelligence and neural networks in Urology: Current clinical applications". In: *Minerva Urologica e Nefrologica* 72.1 (2020), pp. 49–57.

[22] M.B. Christensen, K. Oberg, and J.C. Wolchok. “Tensile properties of the rectal and sigmoid colon: a comparative analysis of human and porcine tissue”. In: *SpringerPlus* 4.1 (2015).

[23] C. Chui et al. “Transversely isotropic properties of porcine liver tissue: Experiments and constitutive modelling”. In: *Medical and Biological Engineering and Computing* 45.1 (2007), pp. 99–106.

[24] Creative Commons. “Attribution-noncommercial-noderivatives 4.0 international (cc by-nc-nd 4.0)”. In: *URL https://creativecommons. org/licenses/by-nc-nd/4.0/.(Accessed: 22.04. 2021)* 92 ().

[25] F. Cornud et al. “TRUS-MRI image registration: A paradigm shift in the diagnosis of significant prostate cancer”. In: *Abdominal Imaging* 38.6 (2013), pp. 1447–1463.

[26] J-M Correas et al. “Ultrasound elastography of the prostate: state of the art”. In: *Diagnostic and interventional imaging* 94.5 (2013), pp. 551–560.

[27] S.E. Dahms et al. “Composition and biomechanical properties of the bladder acellular matrix graft: Comparative analysis in rat, pig and human”. In: *British Journal of Urology* 82.3 (1998), pp. 411–419.

[28] C.J. Das et al. “Mri-targeted prostate biopsy: What radiologists should know”. In: *Korean Journal of Radiology* 21.9 (2020), pp. 1087–1094.

[29] N.B. Delongchamps et al. “Prebiopsy magnetic resonance imaging and prostate cancer detection: Comparison of random and targeted biopsies”. In: *Journal of Urology* 189.2 (2013), pp. 493–499.

[30] Jean-Luc Descotes. “Diagnosis of prostate cancer”. In: *Asian journal of urology* 6.2 (2019), pp. 129–136.

[31] Carmelo Agostino Di Franco et al. “A retrospective comparison between transrectal and transperineal prostate biopsy in the detection of prostate cancer”. In: *Archivio Italiano di Urologia e Andrologia* 89.1 (2017), pp. 55–59.

[32] S. Doll and K. Schweizerhof. “On the development of volumetric strain energy functions”. In: *Journal of Applied Mechanics, Transactions ASME* 67.1 (2000), pp. 17–21.

[33] V.I. Egorov et al. "Mechanical properties of the human gastrointestinal tract". In: *Journal of Biomechanics* 35.10 (2002), pp. 1417–1425.

[34] Alexander E Ehret, Mikhail Itskov, and Georg Weinhold. "A microstructurally motivated anisotropic viscoelastic model for soft tissues". In: *PAMM: Proceedings in Applied Mathematics and Mechanics*. Vol. 8. 1. 2008, pp. 10171–10172.

[35] M. Eklund et al. "MRI-targeted or standard biopsy in prostate cancer screening". In: *New England Journal of Medicine* 385.10 (2021), pp. 908–920.

[36] Electricité de France. *Finite element code_Aster, Analysis of Structures and Thermomechanics for Studies and Research*. Open source on www.code–aster.org. 1989–2017.

[37] P. Emiliozzi et al. "Best approach for prostate cancer detection: A prospective study on transperineal versus transrectal six-core prostate biopsy". In: *Urology* 61.5 (2003), pp. 961–966.

[38] European Commission. *ECIS - European Cancer Information System*. https://ecis.jrc.ec.europa.eu/. Accessed 25-Jun-2021.

[39] A. Fridhammar et al. "The Value of a New Diagnostic Test for Prostate Cancer: A Cost-Utility Analysis in Early Stage of Development". In: *PharmacoEconomics - Open* 5.1 (2021), pp. 77–88.

[40] J. Gao, F. Zhou, and B. Liu. "Elastic image registration of MR/TRUS for targeted prostate biopsy". In: 2013, pp. 245–249.

[41] W.E. Grizzle, W.C. Bell, and K.C. Sexton. "Issues in collecting, processing and storing human tissues and associated information to support biomedical research". In: *Cancer Biomarkers* 9.1-6 (2011), pp. 531–549.

[42] Jeremy P Grummet et al. "Sepsis and 'superbugs': should we favour the transperineal over the transrectal approach for prostate biopsy?" In: *BJU international* 114.3 (2014), pp. 384–388.

[43] G.R. Hale et al. "Comparison of Elastic and Rigid Registration during Magnetic Resonance Imaging/Ultrasound Fusion-Guided Prostate Biopsy: A Multi-Operator Phantom Study". In: *Journal of Urology* 200.5 (2018), pp. 1114–1121.

[44] G. Haskins et al. “Learning deep similarity metric for 3D MR–TRUS image registration”. In: *International Journal of Computer Assisted Radiology and Surgery* 14.3 (2019), pp. 417–425.

[45] T. Helfer et al. “Introducing the open-source mfront code generator: Application to mechanical behaviours and material knowledge management within the PLEIADES fuel element modelling platform”. In: *Computers and Mathematics with Applications* 70.5 (2015), pp. 994–1023.

[46] J.M. Hensel et al. “Development of Multiorgan Finite Element-Based Prostate Deformation Model Enabling Registration of Endorectal Coil Magnetic Resonance Imaging for Radiotherapy Planning”. In: *International Journal of Radiation Oncology Biology Physics* 68.5 (2007), pp. 1522–1528.

[47] G.A. Holzapfel, T.C. Gasser, and M. Stadler. “A structural model for the viscoelastic behavior of arterial walls: Continuum formulation and finite element analysis”. In: *European Journal of Mechanics, A/Solids* 21.3 (2002), pp. 441–463.

[48] Gerhard A Holzapfel. “Nonlinear solid mechanics: a continuum approach for engineering science”. In: *Meccanica* 37.4 (2002), pp. 489–490.

[49] Gerhard A Holzapfel et al. “Biomechanics of soft tissue”. In: *The handbook of materials behavior models* 3.1 (2001), pp. 1049–1063.

[50] K. Hoyt et al. “Tissue elasticity properties as biomarkers for prostate cancer”. In: *Cancer Biomarkers* 4.4-5 (2008), pp. 213–225.

[51] Y. Hu et al. “A comparison of the accuracy of statistical models of prostate motion trained using data from biomechanical simulations”. In: *Progress in Biophysics and Molecular Biology* 103.2-3 (2010), pp. 262–272.

[52] R. Igarasihi et al. “Sagittal alignment in an MR-TRUS fusion biopsy using only the prostate contour in the axial image”. In: *ROBOMECH Journal* 7.1 (2020).

[53] M.T. Islam et al. “Non-invasive imaging of Young’s modulus and Poisson’s ratio in cancers in vivo”. In: *Scientific Reports* 10.1 (2020).

[54] Stepan Janda. “Biomechanics of the pelvic floor musculature”. PhD thesis. TUD Technische Universiteit Delft, 2006.

[55] B. Johnson, S. Campbell, and N. Campbell-Kyureghyan. “The differences in measured prostate material properties between probing and unconfined compression testing methods”. In: *Medical Engineering and Physics* 80 (2020), pp. 44–51.

[56] L. Keros et al. “Qualitative estimation of pelvic organ interactions and their consequences on prostate motion: Study on a deceased person”. In: *Medical Physics* 33.6 (2006), pp. 1902–1910.

[57] S. Korossis et al. “Regional biomechanical and histological characterisation of the passive porcine urinary bladder: Implications for augmentation and tissue engineering strategies”. In: *Biomaterials* 30.2 (2009), pp. 266–275.

[58] T.A. Krouskop et al. “Elastic moduli of breast and prostate tissues under compression”. In: *Ultrasonic Imaging* 20.4 (1998), pp. 260–274.

[59] C. Li et al. “Quantitative elasticity measurement of urinary bladder wall using laser-induced surface acoustic waves”. In: *Biomedical Optics Express* 5.12 (2014), pp. 4313–4328.

[60] S. Lim et al. “Robotic transrectal ultrasound guided prostate biopsy”. In: *IEEE Transactions on Biomedical Engineering* 66 (2019), pp. 2527–2537.

[61] G. Limbert and J. Middleton. “A constitutive model of the posterior cruciate ligament”. In: *Medical Engineering and Physics* 28.2 (2006), pp. 99–113.

[62] G. Limbert and J. Middleton. “An anisotropic viscous hyperelastic constitutive model of the posterior cruciate ligament suitable for high loading rate situations”. In: *Solid Mechanics and its Applications* 124 (2005), pp. 477–483.

[63] H. Liu et al. “Anisotropic finite strain viscoelasticity: Constitutive modeling and finite element implementation”. In: 124 (2019), pp. 172–188.

[64] J. Ma et al. “Prostatic fibrosis is associated with lower urinary tract symptoms”. In: *Journal of Urology* 188.4 (2012), pp. 1375–1381.

[65] A. Maghsoudi and M. Jahed. “Needle dynamics modelling and control in prostate brachytherapy”. In: *IET Control Theory and Applications* 6.11 (2012), pp. 1671–1681.

[66] M. Marchal, E. Promayon, and J. Troccaz. “Simulating prostate surgical procedures with a discrete soft tissue model”. In: 2006, pp. 109–118.

[67] P.A.L.S. Martins et al. "Uniaxial mechanical behavior of the human female bladder". In: *International Urogynecology Journal* 22.8 (2011), pp. 991–995.

[68] D. Massalou et al. "Mechanical effects of load speed on the human colon". In: *Journal of Biomechanics* 91 (2019), pp. 102–108.

[69] K. Miller et al. "Mechanical properties of brain tissue in-vivo: Experiment and computer simulation". In: *Journal of Biomechanics* 33.11 (2000), pp. 1369–1376.

[70] Nobutaka Mitsuhashi et al. "BodyParts3D: 3D structure database for anatomical concepts". In: *Nucleic acids research* 37.suppl_1 (2009), pp. D782–D785.

[71] Andrew Moe and Dickon Hayne. "Transrectal ultrasound biopsy of the prostate: does it still have a role in prostate cancer diagnosis?" In: *Translational Andrology and Urology* 9.6 (2020), p. 3018.

[72] A. Mohamed, C. Davatzikos, and R. Taylor. "A combined statistical and biomechanical model for estimation of intra-operative prostate deformation". In: *Lecture Notes in Computer Science (including subseries Lecture Notes in Artificial Intelligence and Lecture Notes in Bioinformatics)* 2489 (2002), pp. 452–460.

[73] V.C. Mow et al. "Biphasic creep and stress relaxation of articular cartilage in compression: Theory and experiments". In: *Journal of Biomechanical Engineering* 102.1 (1980), pp. 73–84.

[74] T. Muangpoon et al. "Augmented reality system for digital rectal examination training and assessment: System validation". In: *Journal of Medical Internet Research* 22.8 (2020).

[75] J. Palacio-Torralba et al. "Patient specific modeling of palpation-based prostate cancer diagnosis: Effects of pelvic cavity anatomy and intrabladder pressure". In: *International Journal for Numerical Methods in Biomedical Engineering* 32.1 (2016), pp. 1–13.

[76] J. Palacio-Torralba et al. "Quantitative diagnostics of soft tissue through viscoelastic characterization using time-based instrumented palpation". In: *Journal of the Mechanical Behavior of Biomedical Materials* 41 (2015), pp. 149–160.

[77] J. Panzone et al. "Transrectal Ultrasound in Prostate Cancer: Current Utilization, Integration with mpMRI, HIFU and Other Emerging Applications". In: *Cancer Management and Research* 14 (2022), pp. 1209–1228.

[78] M.P.L. Parente et al. "The influence of the material properties on the biomechanical behavior of the pelvic floor muscles during vaginal delivery". In: *Journal of Biomechanics* 42.9 (2009), pp. 1301–1306.

[79] Y. Payan and J. Ohayon. *Biomechanics of Living Organs: Hyperelastic Constitutive Laws for Finite Element Modeling*. 2017, pp. 1–575.

[80] Tobias Penzkofer et al. "Transperineal in-bore 3-T MR imaging–guided prostate biopsy: a prospective clinical observational study". In: *Radiology* 274.1 (2015), pp. 170–180.

[81] P. Pepe et al. "Transperineal Versus Transrectal MRI/TRUS Fusion Targeted Biopsy: Detection Rate of Clinically Significant Prostate Cancer". In: *Clinical Genitourinary Cancer* 15.1 (2017), e33–e36.

[82] S. Phipps et al. "Measurement of tissue mechanical characteristics to distinguish between benign and malignant prostatic disease". In: *Urology* 66.2 (2005), pp. 447–450.

[83] P.A. Pinto et al. "Magnetic resonance imaging/ultrasound fusion guided prostate biopsy improves cancer detection following transrectal ultrasound biopsy and correlates with multiparametric magnetic resonance imaging". In: *Journal of Urology* 186.4 (2011), pp. 1281–1285.

[84] D. Portalez et al. "Validation of the European Society of Urogenital Radiology scoring system for prostate cancer diagnosis on multiparametric magnetic resonance imaging in a cohort of repeat biopsy patients". In: *European Urology* 62.6 (2012), pp. 986–996.

[85] J. Power et al. "Transperineal ultrasound-guided prostate biopsy: what the radiologist needs to know". In: *Insights into Imaging* 13.1 (2022).

[86] A. Prcic, E. Begic, and M. Hiros. "Usefulness of total PSA value in prostate diseases diagnosis". In: *Acta Informatica Medica* 24.3 (2016), pp. 156–161.

[87] PP Provenzano et al. "Application of nonlinear viscoelastic models to describe ligament behavior". In: *Biomechanics and modeling in mechanobiology* 1.1 (2002), pp. 45–57.

[88] Muhammad Qasim et al. “Biomechanical modelling of the pelvic system: improving the accuracy of the location of neoplasms in MRI-TRUS fusion prostate biopsy”. In: *BMC cancer* 22.1 (2022), pp. 1–10.

[89] Y. Qiao et al. “Measurement of mechanical properties of rectal wall”. In: *Journal of Materials Science: Materials in Medicine* 16.2 (2005), pp. 183–188.

[90] M. Ramezani et al. “In Silico Pelvis and Sacroiliac Joint Motion: Refining a Model of the Human Osteoligamentous Pelvis for Assessing Physiological Load Deformation Using an Inverted Validation Approach”. In: *BioMed Research International* 2019 (2019).

[91] M. Ramezani et al. “In Silico Pelvis and Sacroiliac Joint Motion: Refining a Model of the Human Osteoligamentous Pelvis for Assessing Physiological Load Deformation Using an Inverted Validation Approach”. In: *BioMed Research International* 2019 (2019).

[92] P.H.J. Riegman et al. “Characterization of the human kallikrein locus”. In: *Genomics* 14.1 (1992), pp. 6–11.

[93] C. Rubod et al. “Biomechanical properties of human pelvic organs”. In: *Urology* 79.4 (2012), 968.e17–968.e22.

[94] A.M. Ruiz-Zapata et al. “Biomechanical Properties of the Pelvic Floor and its Relation to Pelvic Floor Disorders[Figure presented]”. In: *European Urology, Supplements* 17.3 (2018), pp. 80–90.

[95] Tomokazu Sazuka et al. “Analysis of preoperative detection for apex prostate cancer by transrectal biopsy”. In: *Prostate Cancer* 2013 (2013).

[96] A.-O. Schäfer and M. Langer. *MRI of rectal cancer: Clinical atlas*. 2010, pp. 1–215.

[97] F. Shen et al. “Three-dimensional sonography with needle tracking: Role in diagnosis and treatment of prostate cancer”. In: *Journal of Ultrasound in Medicine* 27.6 (2008), pp. 895–905.

[98] M.M. Siddiqui et al. “Comparison of MR/ultrasound fusion-guided biopsy with ultrasound-guided biopsy for the diagnosis of prostate cancer”. In: *JAMA - Journal of the American Medical Association* 313.4 (2015), pp. 390–397.

[99] J.C. Simo and C. Miehe. “Associative coupled thermoplasticity at finite strains: Formulation, numerical analysis and implementation”. In: *Computer Methods in Applied Mechanics and Engineering* 98.1 (1992), pp. 41–104.

[100] G. Singh and A. Chanda. “Mechanical properties of whole-body soft human tissues: A review”. In: *Biomedical Materials (Bristol)* 16.6 (2021).

[101] Omesh Singh and Srinivasa Rao Bolla. “Anatomy, abdomen and pelvis, prostate”. In: *StatPearls [Internet]*. 2020.

[102] Omesh Singh and Srinivasa Rao Bolla. “Anatomy, abdomen and pelvis, prostate”. In: *StatPearls [Internet]*. 2021.

[103] S. Sinha and U. Sinha. “In vivo diffusion tensor imaging of the human prostate”. In: *Magnetic Resonance in Medicine* 52.3 (2004), pp. 530–537.

[104] J.M. Song et al. “Prostate-specific antigen, digital rectal examination and transrectal ultrasonography: A meta-analysis for this diagnostic triad of prostate cancer in symptomatic Korean men”. In: *Yonsei Medical Journal* 46.3 (2005), pp. 414–424.

[105] G.A. Sonn et al. “Targeted biopsy in the detection of prostate cancer using an office based magnetic resonance ultrasound fusion device”. In: *Journal of Urology* 189.1 (2013), pp. 86–92.

[106] LE Sousa, GS Fernandes, CG Santos, et al. “Knowledge about male pelvis anatomy and prostate cancer in men”. In: *Int J Fam Commun Med* 4.4 (2020), pp. 92–97.

[107] J.P. Spirnak and M.I. Resnick. “Transrectal ultrasonography”. In: *Urology* 23.5 (1984), pp. 461–467.

[108] H. Sung et al. “Global Cancer Statistics 2020: GLOBOCAN Estimates of Incidence and Mortality Worldwide for 36 Cancers in 185 Countries”. In: *CA Cancer Journal for Clinicians* 71.3 (2021), pp. 209–249.

[109] Z.A. Taylor, T.B. Kirk, and K. Miller. “Confocal arthroscopy-based patient-specific constitutive models of cartilaginous tissues-I: Development of a microstructural model”. In: *Computer Methods in Biomechanics and Biomedical Engineering* 10.4 (2007), pp. 307–316.

[110] Z.A. Taylor et al. "On modelling of anisotropic viscoelasticity for soft tissue simulation: Numerical solution and GPU execution". In: *Medical Image Analysis* 13.2 (2009), pp. 234–244.

[111] L.A. Torre et al. "Global cancer statistics, 2012". In: *CA Cancer Journal for Clinicians* 65.2 (2015), pp. 87–108.

[112] B. Turkbey et al. "Prostate Imaging Reporting and Data System Version 2.1: 2019 Update of Prostate Imaging Reporting and Data System Version 2". In: 76.3 (2019), pp. 340–351.

[113] L. Tuset et al. "Implementation of a new constitutive model for abdominal muscles". In: *Computer Methods and Programs in Biomedicine* 179 (2019).

[114] M.D. Vardy et al. "The effects of hormone replacement on the biomechanical properties of the uterosacral and round ligaments in the monkey model". In: *American Journal of Obstetrics and Gynecology* 192.5 SPEC. ISS. (2005), pp. 1741–1751.

[115] N. Wang et al. "Using a prostate exam simulator to decipher palpation techniques that facilitate the detection of abnormalities near clinical limits". In: *Simulation in Healthcare* 5.3 (2010), pp. 152–160.

[116] Y. Wang et al. "Patient-specific Deformation Modelling via Elastography: Application to Image-guided Prostate Interventions". In: *Scientific Reports* 6 (2016).

[117] C. Warlick et al. "Beyond transrectal ultrasound-guided prostate biopsies: available techniques and approaches". In: *World Journal of Urology* 37.3 (2019), pp. 419–427.

[118] S.L.-Y. Woo, G.A. Johnson, and B.A. Smith. "Mathematical modeling of ligaments and tendons". In: *Journal of Biomechanical Engineering* 115.4 (1993), pp. 468–473.

[119] Guorong Wu et al. "Scalable high-performance image registration framework by unsupervised deep feature representations learning". In: *IEEE Transactions on Biomedical Engineering* 63.7 (2015), pp. 1505–1516.

[120] J. Xiang et al. "Transperineal versus transrectal prostate biopsy in the diagnosis of prostate cancer: A systematic review and meta-analysis". In: *World Journal of Surgical Oncology* 17.1 (2019).

[121] S. Xu et al. “Real-time MRI-TRUS fusion for guidance of targeted prostate biopsies”. In: *Computer Aided Surgery* 13.5 (2008), pp. 255–264.

[122] L. Yuan et al. “Comparison of ultrasound-guided transrectal and transperineal prostate biopsies in clinical application”. In: *National journal of andrology* 20.11 (2014), pp. 1004–1007.

[123] John L Zeller, Cassio Lynm, and Richard M Glass. “Grading of prostate cancer”. In: *JAMA* 298.13 (2007), pp. 1596–1596.